

This is the accepted manuscript made available via CHORUS. The article has been published as:

Systematic study of nuclear effects in  $p+Al$ ,  $p+Au$ ,  $d+Au$  collisions at  $\sqrt{s_{NN}} = 200$  GeV using  $\pi^0$  production

U. A. Acharya et al. (PHENIX Collaboration)

Phys. Rev. C **105**, 064902 — Published 6 June 2022

DOI: [10.1103/PhysRevC.105.064902](https://doi.org/10.1103/PhysRevC.105.064902)

1 **Systematic study of nuclear effects in  $p+\text{Al}$ ,  $p+\text{Au}$ ,  $d+\text{Au}$ , and  $^3\text{He}+\text{Au}$  collisions at**  
2  **$\sqrt{s_{NN}} = 200 \text{ GeV}$  using  $\pi^0$  production**

3 U.A. Acharya,<sup>23</sup> A. Adare,<sup>12</sup> C. Aidala,<sup>46,47</sup> N.N. Ajitanand,<sup>69,\*</sup> Y. Akiba,<sup>63,64,†</sup> H. Al-Bataineh,<sup>55</sup> J. Alexander,<sup>69</sup>  
4 M. Alfred,<sup>25</sup> V. Andrieux,<sup>47</sup> A. Angerami,<sup>13</sup> K. Aoki,<sup>34,37,63</sup> N. Apadula,<sup>30,70</sup> Y. Aramaki,<sup>11,63</sup> H. Asano,<sup>37,63</sup>  
5 E.T. Atomssa,<sup>38</sup> R. Averbeck,<sup>70</sup> T.C. Awes,<sup>58</sup> B. Azmoun,<sup>7</sup> V. Babintsev,<sup>26</sup> M. Bai,<sup>6</sup> G. Baksay,<sup>21</sup> L. Baksay,<sup>21</sup>  
6 N.S. Bandara,<sup>46</sup> B. Bannier,<sup>70</sup> K.N. Barish,<sup>8</sup> B. Bassalleck,<sup>54</sup> A.T. Basye,<sup>1</sup> S. Bathe,<sup>5,8,64</sup> V. Baublis,<sup>61</sup>  
7 C. Baumann,<sup>7,48</sup> A. Bazilevsky,<sup>7</sup> M. Beaumier,<sup>8</sup> S. Beckman,<sup>12</sup> S. Belikov,<sup>7,\*</sup> R. Belmont,<sup>12,47,56,76</sup> R. Bennett,<sup>70</sup>  
8 A. Berdnikov,<sup>66</sup> Y. Berdnikov,<sup>66</sup> J.H. Bhom,<sup>80</sup> L. Bichon,<sup>76</sup> B. Blankenship,<sup>76</sup> D.S. Blau,<sup>36,53</sup> J.S. Bok,<sup>55,80</sup>  
9 V. Borisov,<sup>66</sup> K. Boyle,<sup>64,70</sup> M.L. Brooks,<sup>41</sup> J. Bryslawskij,<sup>5,8</sup> H. Buesching,<sup>7</sup> V. Bumazhnov,<sup>26</sup> G. Bunce,<sup>7,64</sup>  
10 S. Butsyk,<sup>41</sup> S. Campbell,<sup>13,30,70</sup> V. Canoa Roman,<sup>70</sup> A. Caringi,<sup>49</sup> R. Cervantes,<sup>70</sup> C.-H. Chen,<sup>64,70</sup> M. Chiu,<sup>7</sup>  
11 C.Y. Chi,<sup>13</sup> I.J. Choi,<sup>27,80</sup> J.B. Choi,<sup>32,\*</sup> R.K. Choudhury,<sup>4</sup> P. Christiansen,<sup>43</sup> T. Chujo,<sup>75</sup> P. Chung,<sup>69</sup>  
12 O. Chvala,<sup>8</sup> V. Cianciolo,<sup>58</sup> Z. Citron,<sup>70,78</sup> B.A. Cole,<sup>13</sup> Z. Conesa del Valle,<sup>38</sup> M. Connors,<sup>23,64,70</sup>  
13 R. Corliss,<sup>70</sup> Y. Corrales Morales,<sup>41</sup> N. Cronin,<sup>49,70</sup> T. Csörgő,<sup>18,79</sup> M. Csanád,<sup>17</sup> L. D’Orazio,<sup>45</sup> T. Dahms,<sup>70</sup>  
14 S. Dairaku,<sup>37,63</sup> I. Danchev,<sup>76</sup> T.W. Danley,<sup>57</sup> K. Das,<sup>22</sup> A. Datta,<sup>46,54</sup> M.S. Daugherty,<sup>1</sup> G. David,<sup>7,70</sup>  
15 M.K. Dayananda,<sup>23</sup> C.T. Dean,<sup>41</sup> K. DeBlasio,<sup>54</sup> K. Dehmelt,<sup>70</sup> A. Denisov,<sup>26</sup> A. Deshpande,<sup>64,70</sup> E.J. Desmond,<sup>7</sup>  
16 K.V. Dharmawardane,<sup>55</sup> O. Dietzsch,<sup>67</sup> A. Dion,<sup>30,70</sup> P.B. Diss,<sup>45</sup> D. Dixit,<sup>70</sup> M. Donadelli,<sup>67</sup> J.H. Do,<sup>80</sup>  
17 V. Doomra,<sup>70</sup> O. Drapier,<sup>38</sup> A. Drees,<sup>70</sup> K.A. Drees,<sup>6</sup> J.M. Durham,<sup>41,70</sup> A. Durum,<sup>26</sup> D. Dutta,<sup>4</sup> S. Edwards,<sup>22</sup>  
18 Y.V. Efremenko,<sup>58</sup> F. Ellinghaus,<sup>12</sup> H. En’yo,<sup>63,64</sup> T. Engelmores,<sup>13</sup> A. Enokizono,<sup>58,63,65</sup> R. Esha,<sup>70</sup> S. Esumi,<sup>75</sup>  
19 B. Fadem,<sup>49</sup> W. Fan,<sup>70</sup> N. Feege,<sup>70</sup> D.E. Fields,<sup>54</sup> M. Finger, Jr.,<sup>9</sup> M. Finger,<sup>9</sup> D. Fitzgerald,<sup>47</sup> F. Fleuret,<sup>38</sup>  
20 S.L. Fokin,<sup>36</sup> Z. Fraenkel,<sup>78,\*</sup> J.E. Frantz,<sup>57,70</sup> A. Franz,<sup>7</sup> A.D. Frawley,<sup>22</sup> K. Fujiwara,<sup>63</sup> Y. Fukao,<sup>63</sup> Y. Fukuda,<sup>75</sup>  
21 T. Fusayasu,<sup>51</sup> P. Gallus,<sup>14</sup> C. Gal,<sup>70</sup> P. Garg,<sup>3,70</sup> I. Garishvili,<sup>40,72</sup> H. Ge,<sup>70</sup> M. Giles,<sup>70</sup> F. Giordano,<sup>27</sup> A. Glenn,<sup>40</sup>  
22 H. Gong,<sup>70</sup> M. Gonin,<sup>38</sup> Y. Goto,<sup>63,64</sup> R. Granier de Cassagnac,<sup>38</sup> N. Grau,<sup>2,13</sup> S.V. Greene,<sup>76</sup> G. Grim,<sup>41</sup>  
23 M. Grosse Perdekamp,<sup>27</sup> T. Gunji,<sup>11</sup> H. Guragain,<sup>23</sup> H.-A+A. Gustafsson,<sup>43,\*</sup> T. Hachiya,<sup>52,63,64</sup> J.S. Haggerty,<sup>7</sup>  
24 K.I. Hahn,<sup>19</sup> H. Hamagaki,<sup>11</sup> J. Hamblen,<sup>72</sup> H.F. Hamilton,<sup>1</sup> J. Hanks,<sup>13,70</sup> R. Han,<sup>60</sup> S.Y. Han,<sup>19,35</sup> M. Harvey,<sup>73</sup>  
25 S. Hasegawa,<sup>31</sup> T.O.S. Haseler,<sup>23</sup> K. Hashimoto,<sup>63,65</sup> E. Haslum,<sup>43</sup> R. Hayano,<sup>11</sup> M. Heffner,<sup>40</sup> T.K. Hemmick,<sup>70</sup>  
26 T. Hester,<sup>8</sup> X. He,<sup>23</sup> J.C. Hill,<sup>30</sup> K. Hill,<sup>12</sup> A. Hodges,<sup>23</sup> M. Hohlmann,<sup>21</sup> R.S. Hollis,<sup>8</sup> W. Holzmann,<sup>13</sup> K. Homma,<sup>24</sup>  
27 B. Hong,<sup>35</sup> T. Horaguchi,<sup>24</sup> D. Hornback,<sup>72</sup> T. Hoshino,<sup>24</sup> N. Hotvedt,<sup>30</sup> J. Huang,<sup>7</sup> T. Ichihara,<sup>63,64</sup> R. Ichimiya,<sup>63</sup>  
28 Y. Ikeda,<sup>75</sup> K. Imai,<sup>31,37,63</sup> M. Inaba,<sup>75</sup> A. Iordanova,<sup>8</sup> D. Isenhower,<sup>1</sup> M. Ishihara,<sup>63</sup> M. Issah,<sup>76</sup> D. Ivanishchev,<sup>61</sup>  
29 Y. Iwanaga,<sup>24</sup> B.V. Jacak,<sup>70</sup> M. Jezghani,<sup>23</sup> X. Jiang,<sup>41</sup> J. Jin,<sup>13</sup> Z. Ji,<sup>70</sup> B.M. Johnson,<sup>7,23</sup> T. Jones,<sup>1</sup> K.S. Joo,<sup>50</sup>  
30 D. Jouan,<sup>59</sup> D.S. Jumper,<sup>1,27</sup> F. Kajihara,<sup>11</sup> J. Kamin,<sup>70</sup> S. Kanda,<sup>11</sup> J.H. Kang,<sup>80</sup> D. Kapukchyan,<sup>8</sup>  
31 J. Kapustinsky,<sup>41</sup> K. Karatsu,<sup>37,63</sup> S. Karthas,<sup>70</sup> M. Kasai,<sup>63,65</sup> D. Kawall,<sup>46,64</sup> M. Kawashima,<sup>63,65</sup>  
32 A.V. Kazantsev,<sup>36</sup> T. Kempel,<sup>30</sup> J.A. Key,<sup>54</sup> V. Khachatryan,<sup>70</sup> A. Khazadzev,<sup>61</sup> A. Khatiwada,<sup>41</sup> K.M. Kijima,<sup>24</sup>  
33 J. Kikuchi,<sup>77</sup> B. Kimelman,<sup>49</sup> A. Kim,<sup>19</sup> B.I. Kim,<sup>35</sup> C. Kim,<sup>8,35</sup> D.J. Kim,<sup>33</sup> E.-J. Kim,<sup>32</sup> G.W. Kim,<sup>19</sup> M. Kim,<sup>68</sup>  
34 T. Kim,<sup>19</sup> Y.-J. Kim,<sup>27</sup> D. Kincses,<sup>17</sup> A. Kingan,<sup>70</sup> E. Kinney,<sup>12</sup> Á. Kiss,<sup>17</sup> E. Kistenev,<sup>7</sup> R. Kitamura,<sup>11</sup>  
35 J. Klatsky,<sup>22</sup> D. Kleinjan,<sup>8</sup> P. Kline,<sup>70</sup> T. Koblesky,<sup>12</sup> L. Kochenda,<sup>61</sup> B. Komkov,<sup>61</sup> M. Konno,<sup>75</sup> J. Koster,<sup>27</sup>  
36 D. Kotov,<sup>61,66</sup> A. Král,<sup>14</sup> A. Kravitz,<sup>13</sup> S. Kudo,<sup>75</sup> G.J. Kunde,<sup>41</sup> K. Kurita,<sup>63,65</sup> M. Kurosawa,<sup>63,64</sup> Y. Kwon,<sup>80</sup>  
37 G.S. Kyle,<sup>55</sup> Y.S. Lai,<sup>13</sup> J.G. Lajoie,<sup>30</sup> D. Larionova,<sup>66</sup> A. Lebedev,<sup>30</sup> D.M. Lee,<sup>41</sup> J. Lee,<sup>19,71</sup> K.B. Lee,<sup>35</sup>  
38 K.S. Lee,<sup>35</sup> S. Lee,<sup>80</sup> S.H. Lee,<sup>30,47,70</sup> M.J. Leitch,<sup>41</sup> M.A.L. Leite,<sup>67</sup> Y.H. Leung,<sup>70</sup> N.A. Lewis,<sup>47</sup> T. Liška,<sup>14</sup>  
39 P. Lichtenwalner,<sup>49</sup> P. Liebing,<sup>64</sup> S.H. Lim,<sup>41,62,80</sup> L.A. Linden Levy,<sup>12</sup> H. Liu,<sup>41</sup> M.X. Liu,<sup>41</sup> X. Li,<sup>10</sup> X. Li,<sup>41</sup>  
40 V.-R. Loggins,<sup>27</sup> D.A. Loomis,<sup>47</sup> K. Lovasz,<sup>16</sup> B. Love,<sup>76</sup> D. Lynch,<sup>7</sup> S. Lökös,<sup>17</sup> C.F. Maguire,<sup>76</sup> T. Majoros,<sup>16</sup>  
41 Y.I. Makdisi,<sup>6</sup> M. Makek,<sup>81</sup> M.D. Malik,<sup>54</sup> A. Manion,<sup>70</sup> V.I. Manko,<sup>36</sup> E. Mannel,<sup>7,13</sup> Y. Mao,<sup>60,63</sup> H. Masui,<sup>75</sup>  
42 F. Matathias,<sup>13</sup> M. McCumber,<sup>41,70</sup> P.L. McGaughey,<sup>41</sup> D. McGlinchey,<sup>12,22,41</sup> C. McKinney,<sup>27</sup> N. Means,<sup>70</sup>  
43 A. Meles,<sup>55</sup> M. Mendoza,<sup>8</sup> B. Meredith,<sup>27</sup> Y. Miake,<sup>75</sup> T. Mibe,<sup>34</sup> A.C. Mignerey,<sup>45</sup> K. Miki,<sup>63,75</sup> A. Milov,<sup>7,78</sup>  
44 D.K. Mishra,<sup>4</sup> J.T. Mitchell,<sup>7</sup> M. Mitrnkova,<sup>66</sup> Iu. Mitrnkov,<sup>66</sup> G. Mitsuka,<sup>34,64</sup> S. Miyasaka,<sup>63,74</sup> S. Mizuno,<sup>63,75</sup>  
45 A.K. Mohanty,<sup>4</sup> M.M. Mondal,<sup>70</sup> P. Montuenga,<sup>27</sup> H.J. Moon,<sup>50</sup> T. Moon,<sup>35,80</sup> Y. Morino,<sup>11</sup> A. Morreale,<sup>8</sup>  
46 D.P. Morrison,<sup>7</sup> T.V. Moukhanova,<sup>36</sup> B. Mulilo,<sup>35,63</sup> T. Murakami,<sup>37,63</sup> J. Murata,<sup>63,65</sup> A. Mwai,<sup>69</sup> K. Nagai,<sup>74</sup>  
47 S. Nagamiya,<sup>34,63</sup> K. Nagashima,<sup>24</sup> T. Nagashima,<sup>65</sup> J.L. Nagle,<sup>12</sup> M. Naglis,<sup>78</sup> M.I. Nagy,<sup>17,79</sup> I. Nakagawa,<sup>63,64</sup>  
48 H. Nakagomi,<sup>63,75</sup> Y. Nakamiya,<sup>24</sup> K.R. Nakamura,<sup>37,63</sup> T. Nakamura,<sup>63</sup> K. Nakano,<sup>63,74</sup> S. Nam,<sup>19</sup> C. Nattress,<sup>72</sup>  
49 S. Nelson,<sup>20</sup> P.K. Netrakanti,<sup>4</sup> J. Newby,<sup>40</sup> M. Nguyen,<sup>70</sup> M. Nihashi,<sup>24</sup> T. Niida,<sup>75</sup> S. Nishimura,<sup>11</sup> R. Nouicer,<sup>7,64</sup>  
50 T. Novák,<sup>18,79</sup> N. Novitzky,<sup>33,70,75</sup> G. Nukazuka,<sup>63,64</sup> A.S. Nyanin,<sup>36</sup> E. O’Brien,<sup>7</sup> C. Oakley,<sup>23</sup> S.X. Oda,<sup>11</sup>  
51 C.A. Ogilvie,<sup>30</sup> K. Okada,<sup>64</sup> M. Oka,<sup>75</sup> Y. Onuki,<sup>63</sup> J.D. Orjuela Koop,<sup>12</sup> J.D. Osborn,<sup>47,58</sup> A. Oskarsson,<sup>43</sup>  
52 G.J. Ottino,<sup>54</sup> M. Ouchida,<sup>24,63</sup> K. Ozawa,<sup>11,34,75</sup> R. Pak,<sup>7</sup> V. Pantuev,<sup>28,70</sup> V. Papavassiliou,<sup>55</sup> I.H. Park,<sup>19,71</sup>

<sup>53</sup> J.S. Park,<sup>68</sup> S. Park,<sup>63,68,70</sup> S.K. Park,<sup>35</sup> W.J. Park,<sup>35</sup> M. Patel,<sup>30</sup> S.F. Pate,<sup>55</sup> H. Pei,<sup>30</sup> J.-C. Peng,<sup>27</sup> W. Peng,<sup>76</sup>  
<sup>54</sup> H. Pereira,<sup>15</sup> D.V. Perepelitsa,<sup>7,12</sup> G.D.N. Perera,<sup>55</sup> D.Yu. Peressounko,<sup>36</sup> C.E. PerezLara,<sup>70</sup> J. Perry,<sup>30</sup> R. Petti,<sup>7,70</sup>  
<sup>55</sup> M. Phipps,<sup>7,27</sup> C. Pinkenburg,<sup>7</sup> R. Pinson,<sup>1</sup> R.P. Pisani,<sup>7</sup> M. Potekhin,<sup>7</sup> M. Proissl,<sup>70</sup> A. Pun,<sup>57</sup> M.L. Purschke,<sup>7</sup>  
<sup>56</sup> H. Qu,<sup>23</sup> P.V. Radzevich,<sup>66</sup> J. Rak,<sup>33</sup> N. Ramasubramanian,<sup>70</sup> B.J. Ramson,<sup>47</sup> I. Ravinovich,<sup>78</sup> K.F. Read,<sup>58,72</sup>  
<sup>57</sup> S. Rembeczki,<sup>21</sup> K. Reygers,<sup>48</sup> D. Reynolds,<sup>69</sup> V. Riabov,<sup>53,61</sup> Y. Riabov,<sup>61,66</sup> E. Richardson,<sup>45</sup> D. Richford,<sup>5</sup>  
<sup>58</sup> T. Rinn,<sup>27,30</sup> D. Roach,<sup>76</sup> G. Roche,<sup>42,\*</sup> S.D. Rolnick,<sup>8</sup> M. Rosati,<sup>30</sup> S.S.E. Rosendahl,<sup>43</sup> C.A. Rosen,<sup>12</sup> Z. Rowan,<sup>5</sup>  
<sup>59</sup> P. Ružička,<sup>29</sup> J.G. Rubin,<sup>47</sup> J. Runchey,<sup>30</sup> A.S. Safonov,<sup>66</sup> B. Sahlmueller,<sup>48,70</sup> N. Saito,<sup>34</sup> T. Sakaguchi,<sup>7</sup>  
<sup>60</sup> K. Sakashita,<sup>63,74</sup> H. Sako,<sup>31</sup> V. Samsonov,<sup>53,61</sup> S. Sano,<sup>11,77</sup> M. Sarsour,<sup>23</sup> S. Sato,<sup>31,34</sup> T. Sato,<sup>75</sup> S. Sawada,<sup>34</sup>  
<sup>61</sup> B. Schaefer,<sup>76</sup> B.K. Schmoll,<sup>72</sup> K. Sedgwick,<sup>8</sup> J. Seele,<sup>12</sup> R. Seidl,<sup>27,63,64</sup> A. Sen,<sup>30,72</sup> R. Seto,<sup>8</sup> P. Sett,<sup>4</sup>  
<sup>62</sup> A. Sexton,<sup>45</sup> D. Sharma,<sup>70,78</sup> D. Sharma,<sup>70,78</sup> I. Shein,<sup>26</sup> T.-A. Shibata,<sup>63,74</sup> K. Shigaki,<sup>24</sup> M. Shimomura,<sup>30,52,75</sup>  
<sup>63</sup> T. Shioya,<sup>75</sup> K. Shoji,<sup>37,63</sup> P. Shukla,<sup>4</sup> A. Sickles,<sup>7,27</sup> C.L. Silva,<sup>30,41</sup> D. Silvermyr,<sup>43,58</sup> C. Silvestre,<sup>15</sup> K.S. Sim,<sup>35</sup>  
<sup>64</sup> B.K. Singh,<sup>3</sup> C.P. Singh,<sup>3</sup> V. Singh,<sup>3</sup> M. Slunečka,<sup>9</sup> K.L. Smith,<sup>22</sup> M. Snowball,<sup>41</sup> R.A. Soltz,<sup>40</sup> W.E. Sondheim,<sup>41</sup>  
<sup>65</sup> S.P. Sorensen,<sup>72</sup> I.V. Sourikova,<sup>7</sup> P.W. Stankus,<sup>58</sup> E. Stenlund,<sup>43</sup> M. Stepanov,<sup>46,55,\*</sup> S.P. Stoll,<sup>7</sup> T. Sugitate,<sup>24</sup>  
<sup>66</sup> A. Sukhanov,<sup>7</sup> T. Sumita,<sup>63</sup> J. Sun,<sup>70</sup> Z. Sun,<sup>16</sup> J. Sziklai,<sup>79</sup> E.M. Takagui,<sup>67</sup> A. Taketani,<sup>63,64</sup> R. Tanabe,<sup>75</sup>  
<sup>67</sup> Y. Tanaka,<sup>51</sup> S. Taneja,<sup>70</sup> K. Tanida,<sup>31,37,63,64,68</sup> M.J. Tannenbaum,<sup>7</sup> S. Tarafdar,<sup>3,76,78</sup> A. Taranenko,<sup>53,69</sup>  
<sup>68</sup> G. Tarnai,<sup>16</sup> H. Themann,<sup>70</sup> D. Thomas,<sup>1</sup> T.L. Thomas,<sup>54</sup> R. Tieulent,<sup>23,44</sup> A. Timilsina,<sup>30</sup> T. Todoroki,<sup>63,64,75</sup>  
<sup>69</sup> M. Togawa,<sup>64</sup> A. Toia,<sup>70</sup> L. Tomášek,<sup>29</sup> M. Tomášek,<sup>14,29</sup> H. Torii,<sup>24</sup> C.L. Towell,<sup>1</sup> R. Towell,<sup>1</sup> R.S. Towell,<sup>1</sup>  
<sup>70</sup> I. Tserruya,<sup>78</sup> Y. Tsuchimoto,<sup>24</sup> Y. Ueda,<sup>24</sup> B. Ujvari,<sup>16</sup> R. Vértesi,<sup>79</sup> C. Vale,<sup>7</sup> H. Valle,<sup>76</sup> H.W. van Hecke,<sup>41</sup>  
<sup>71</sup> E. Vazquez-Zambrano,<sup>13</sup> A. Veicht,<sup>13,27</sup> J. Velkovska,<sup>76</sup> M. Virius,<sup>14</sup> V. Vrba,<sup>14,29</sup> N. Vukman,<sup>81</sup> E. Vznuzdaev,<sup>61</sup>  
<sup>72</sup> X.R. Wang,<sup>55,64</sup> D. Watanabe,<sup>24</sup> K. Watanabe,<sup>75</sup> Y. Watanabe,<sup>63,64</sup> Y.S. Watanabe,<sup>11,34</sup> F. Wei,<sup>30,55</sup> R. Wei,<sup>69</sup>  
<sup>73</sup> J. Wessels,<sup>48</sup> A.S. White,<sup>47</sup> S.N. White,<sup>7</sup> D. Winter,<sup>13</sup> C.P. Wong,<sup>23,41</sup> C.L. Woody,<sup>7</sup> R.M. Wright,<sup>1</sup>  
<sup>74</sup> M. Wysocki,<sup>12,58</sup> B. Xia,<sup>57</sup> L. Xue,<sup>23</sup> C. Xu,<sup>55</sup> Q. Xu,<sup>76</sup> S. Yalcin,<sup>70</sup> Y.L. Yamaguchi,<sup>11,63,70</sup> H. Yamamoto,<sup>75</sup>  
<sup>75</sup> K. Yamaura,<sup>24</sup> R. Yang,<sup>27</sup> A. Yanovich,<sup>26</sup> J. Ying,<sup>23</sup> S. Yokkaichi,<sup>63,64</sup> I. Yoon,<sup>68</sup> J.H. Yoo,<sup>35</sup> G.R. Young,<sup>58</sup>  
<sup>76</sup> I. Younus,<sup>39,54</sup> Z. You,<sup>60</sup> I.E. Yushmanov,<sup>36</sup> H. Yu,<sup>55,60</sup> W.A. Zajc,<sup>13</sup> A. Zelenski,<sup>6</sup> S. Zhou,<sup>10</sup> and L. Zou<sup>8</sup>

(PHENIX Collaboration)

<sup>1</sup>Abilene Christian University, Abilene, Texas 79699, USA

<sup>2</sup>Department of Physics, Augustana University, Sioux Falls, South Dakota 57197, USA

<sup>3</sup>Department of Physics, Banaras Hindu University, Varanasi 221005, India

<sup>4</sup>Bhabha Atomic Research Centre, Bombay 400 085, India

<sup>5</sup>Baruch College, City University of New York, New York, New York, 10010 USA

<sup>6</sup>Collider-Accelerator Department, Brookhaven National Laboratory, Upton, New York 11973-5000, USA

<sup>7</sup>Physics Department, Brookhaven National Laboratory, Upton, New York 11973-5000, USA

<sup>8</sup>University of California-Riverside, Riverside, California 92521, USA

<sup>9</sup>Charles University, Ovocný trh 5, Praha 1, 116 36, Prague, Czech Republic

<sup>10</sup>Science and Technology on Nuclear Data Laboratory, China Institute of Atomic Energy, Beijing 102413, People's Republic of China

<sup>11</sup>Center for Nuclear Study, Graduate School of Science, University of Tokyo, 7-3-1 Hongo, Bunkyo, Tokyo 113-0033, Japan

<sup>12</sup>University of Colorado, Boulder, Colorado 80309, USA

<sup>13</sup>Columbia University, New York, New York 10027 and Nevis Laboratories, Irvington, New York 10533, USA

<sup>14</sup>Czech Technical University, Zikova 4, 166 36 Prague 6, Czech Republic

<sup>15</sup>Dapnia, CEA Saclay, F-91191, Gif-sur-Yvette, France

<sup>16</sup>Debrecen University, H-4010 Debrecen, Egyetem tér 1, Hungary

<sup>17</sup>ELTE, Eötvös Loránd University, H-1117 Budapest, Pázmány P. s. 1/A, Hungary

<sup>18</sup>Eszterházy Károly University, Károly Róbert Campus, H-3200 Gyöngyös, Mátrai út 36, Hungary

<sup>19</sup>Ewha Womans University, Seoul 120-750, Korea

<sup>20</sup>Florida A&M University, Tallahassee, FL 32307, USA

<sup>21</sup>Florida Institute of Technology, Melbourne, Florida 32901, USA

<sup>22</sup>Florida State University, Tallahassee, Florida 32306, USA

<sup>23</sup>Georgia State University, Atlanta, Georgia 30303, USA

<sup>24</sup>Hiroshima University, Kagamiyama, Higashi-Hiroshima 739-8526, Japan

<sup>25</sup>Department of Physics and Astronomy, Howard University, Washington, DC 20059, USA

<sup>26</sup>IHEP Protvino, State Research Center of Russian Federation, Institute for High Energy Physics, Protvino, 142281, Russia

<sup>27</sup>University of Illinois at Urbana-Champaign, Urbana, Illinois 61801, USA

<sup>28</sup>Institute for Nuclear Research of the Russian Academy of Sciences, prospekt 60-letiya Oktyabrya 7a, Moscow 117312, Russia

<sup>29</sup>Institute of Physics, Academy of Sciences of the Czech Republic, Na Slovance 2, 182 21 Prague 8, Czech Republic

<sup>30</sup>Iowa State University, Ames, Iowa 50011, USA

<sup>31</sup>Advanced Science Research Center, Japan Atomic Energy Agency, 2-4

Shirakata Shirane, Tokai-mura, Naka-gun, Ibaraki-ken 319-1195, Japan

<sup>32</sup>Jeonbuk National University, Jeonju, 54896, Korea

- 112 <sup>33</sup>Helsinki Institute of Physics and University of Jyväskylä, P.O.Box 35, FI-40014 Jyväskylä, Finland  
 113 <sup>34</sup>KEK, High Energy Accelerator Research Organization, Tsukuba, Ibaraki 305-0801, Japan  
 114 <sup>35</sup>Korea University, Seoul 02841, Korea  
 115 <sup>36</sup>National Research Center “Kurchatov Institute”, Moscow, 123098 Russia  
 116 <sup>37</sup>Kyoto University, Kyoto 606-8502, Japan  
 117 <sup>38</sup>Laboratoire Leprince-Ringuet, Ecole Polytechnique, CNRS-IN2P3, Route de Saclay, F-91128, Palaiseau, France  
 118 <sup>39</sup>Physics Department, Lahore University of Management Sciences, Lahore 54792, Pakistan  
 119 <sup>40</sup>Lawrence Livermore National Laboratory, Livermore, California 94550, USA  
 120 <sup>41</sup>Los Alamos National Laboratory, Los Alamos, New Mexico 87545, USA  
 121 <sup>42</sup>LPC, Université Blaise Pascal, CNRS-IN2P3, Clermont-Fd, 63177 Aubiere Cedex, France  
 122 <sup>43</sup>Department of Physics, Lund University, Box 118, SE-221 00 Lund, Sweden  
 123 <sup>44</sup>IPNL, CNRS/IN2P3, Univ Lyon, Université Lyon 1, F-69622, Villeurbanne, France  
 124 <sup>45</sup>University of Maryland, College Park, Maryland 20742, USA  
 125 <sup>46</sup>Department of Physics, University of Massachusetts, Amherst, Massachusetts 01003-9337, USA  
 126 <sup>47</sup>Department of Physics, University of Michigan, Ann Arbor, Michigan 48109-1040, USA  
 127 <sup>48</sup>Institut für Kernphysik, University of Münster, D-48149 Münster, Germany  
 128 <sup>49</sup>Muhlenberg College, Allentown, Pennsylvania 18104-5586, USA  
 129 <sup>50</sup>Myongji University, Yongin, Kyonggido 449-728, Korea  
 130 <sup>51</sup>Nagasaki Institute of Applied Science, Nagasaki-shi, Nagasaki 851-0193, Japan  
 131 <sup>52</sup>Nara Women’s University, Kita-uoya Nishi-machi Nara 630-8506, Japan  
 132 <sup>53</sup>National Research Nuclear University, MEPhI, Moscow Engineering Physics Institute, Moscow, 115409, Russia  
 133 <sup>54</sup>University of New Mexico, Albuquerque, New Mexico 87131, USA  
 134 <sup>55</sup>New Mexico State University, Las Cruces, New Mexico 88003, USA  
 135 <sup>56</sup>Physics and Astronomy Department, University of North Carolina at Greensboro, Greensboro, North Carolina 27412, USA  
 136 <sup>57</sup>Department of Physics and Astronomy, Ohio University, Athens, Ohio 45701, USA  
 137 <sup>58</sup>Oak Ridge National Laboratory, Oak Ridge, Tennessee 37831, USA  
 138 <sup>59</sup>IPN-Orsay, Univ. Paris-Sud, CNRS/IN2P3, Université Paris-Saclay, BP1, F-91406, Orsay, France  
 139 <sup>60</sup>Peking University, Beijing 100871, People’s Republic of China  
 140 <sup>61</sup>PNPI, Petersburg Nuclear Physics Institute, Gatchina, Leningrad region, 188300, Russia  
 141 <sup>62</sup>Pusan National University, Pusan 46241, Korea  
 142 <sup>63</sup>RIKEN Nishina Center for Accelerator-Based Science, Wako, Saitama 351-0198, Japan  
 143 <sup>64</sup>RIKEN BNL Research Center, Brookhaven National Laboratory, Upton, New York 11973-5000, USA  
 144 <sup>65</sup>Physics Department, Rikkyo University, 3-34-1 Nishi-Ikebukuro, Toshima, Tokyo 171-8501, Japan  
 145 <sup>66</sup>Saint Petersburg State Polytechnic University, St. Petersburg, 195251 Russia  
 146 <sup>67</sup>Universidade de São Paulo, Instituto de Física, Caixa Postal 66318, São Paulo CEP05315-970, Brazil  
 147 <sup>68</sup>Department of Physics and Astronomy, Seoul National University, Seoul 151-742, Korea  
 148 <sup>69</sup>Chemistry Department, Stony Brook University, SUNY, Stony Brook, New York 11794-3400, USA  
 149 <sup>70</sup>Department of Physics and Astronomy, Stony Brook University, SUNY, Stony Brook, New York 11794-3800, USA  
 150 <sup>71</sup>Sungkyunkwan University, Suwon, 440-746, Korea  
 151 <sup>72</sup>University of Tennessee, Knoxville, Tennessee 37996, USA  
 152 <sup>73</sup>Texas Southern University, Houston, TX 77004, USA  
 153 <sup>74</sup>Department of Physics, Tokyo Institute of Technology, Oh-okayama, Meguro, Tokyo 152-8551, Japan  
 154 <sup>75</sup>Tomonaga Center for the History of the Universe, University of Tsukuba, Tsukuba, Ibaraki 305, Japan  
 155 <sup>76</sup>Vanderbilt University, Nashville, Tennessee 37235, USA  
 156 <sup>77</sup>Waseda University, Advanced Research Institute for Science and  
 157 Engineering, 17 Kikui-cho, Shinjuku-ku, Tokyo 162-0044, Japan  
 158 <sup>78</sup>Weizmann Institute, Rehovot 76100, Israel  
 159 <sup>79</sup>Institute for Particle and Nuclear Physics, Wigner Research Centre for Physics, Hungarian  
 160 Academy of Sciences (Wigner RCP, RMKI) H-1525 Budapest 114, POBox 49, Budapest, Hungary  
 161 <sup>80</sup>Yonsei University, IPAP, Seoul 120-749, Korea  
 162 <sup>81</sup>Department of Physics, Faculty of Science, University of Zagreb, Bijenička c. 32 HR-10002 Zagreb, Croatia  
 163 (Dated: May 3, 2022)

164 The PHENIX collaboration presents a systematic study of **inclusive**  $\pi^0$  production from  $p+p$ ,  
 165  $p+Al$ ,  $p+Au$ ,  $d+Au$ , and  $^3He+Au$  collisions at  $\sqrt{s_{NN}} = 200$  GeV. Measurements were performed  
 166 with different centrality selections as well as the total inelastic, 0%–100%, selection for all collision  
 167 systems. For 0%–100% collisions, the nuclear-modification factors,  $R_{xA}$ , are consistent with unity  
 168 for  $p_T$  above 8 GeV/c, but exhibit an enhancement in peripheral collisions and a suppression in  
 169 central collisions. The enhancement and suppression characteristics are similar for all systems for  
 170 the same centrality class. It is shown that for high- $p_T$ - $\pi^0$  production, the nucleons in the  $d$  and  
 171  $^3He$  interact mostly independently with the Au nucleus and that the counter intuitive centrality  
 172 dependence is likely due to a physical correlation between multiplicity and the presence of a hard  
 173 scattering process. These observations disfavor models where parton energy loss has a significant  
 174 contribution to nuclear modifications in small systems. Nuclear modifications at lower  $p_T$  resemble

175 the Cronin effect – an increase followed by a peak in central or inelastic collisions and a plateau in  
 176 peripheral collisions. The peak height has a characteristic ordering by system size as  $p+\text{Au} > d+\text{Au}$   
 177  $> {}^3\text{He}+\text{Au} > p+\text{Al}$ . For collisions with Au ions, current calculations based on initial state cold  
 178 nuclear matter effects result in the opposite order, suggesting the presence of other contributions to  
 179 nuclear modifications, in particular at lower  $p_T$ .

## 180 I. INTRODUCTION

181 Measurements of transverse-momentum ( $p_T$ ) distributions of particles produced in hadronic collisions are commonly  
 182 used to obtain information from the interaction. At the Relativistic Heavy Ion Collider (RHIC) at Brookhaven  
 183 National Laboratory, studies of the nuclear-modification factor  $R_{AA}$  of hadrons, defined as the ratio of the hadron  
 184 yield per binary nucleon-nucleon collision in a given A+A system to the yield measured in  $p+p$  collisions, have led to  
 185 significant insights. The discovery of the suppression of high  $p_T$  neutral pions and charged hadrons [1, 2] in Au+Au  
 186 collisions relative to scaled  $p+p$  collisions at the same energy, was one of the first hints of parton energy loss in the  
 187 strongly coupled quark gluon plasma (QGP). The apparent absence of any suppression in reference spectra from  
 188  $d+\text{Au}$  collisions [3, 4], where the formation of QGP was not expected, was critical to establish parton energy loss as  
 189 the origin of the observed suppression in Au+Au collisions. The subsequent systematic studies of the suppression  
 190 pattern of  $\pi^0$  production in Au+Au collisions at  $\sqrt{s_{NN}} = 200$  GeV allowed for quantitative constraints on the medium  
 191 transport coefficients [5, 6].

192 Experimentally, evidence for cold-nuclear-matter effects was first observed in the late 1970s when the ratio of the  
 193 production cross sections of hadrons from  $p+A$  to  $p+p$  was found to vary with  $p_T$  [7, 8]. This variation was referred  
 194 to as the ‘‘Cronin effect’’: a suppression at low  $p_T$  followed by an enhancement around 2–5 GeV/ $c$  that vanishes  
 195 towards larger  $p_T$ . Historically the Cronin effect was attributed to initial state hard scattering [9, 10], but this  
 196 explanation remained unsatisfactory because it could not explain the much larger effect for protons compared to  
 197 pions. Measurements of the momentum spectra at RHIC in the early 2000s renewed interest in the Cronin effect,  
 198 and various theoretical models have been developed to explain it. Most models were based on hard and soft multiple  
 199 scattering [11–15], but there were additional approaches involving gluon saturation [16] or hadronization by quark  
 200 recombination [17]. To date, there is no full quantitative explanation of the Cronin effect.

201 There are striking similarities between long range particle correlations in A+A collisions and those observed in high  
 202 multiplicity  $p+p$  and  $p+\text{Pb}$  collisions at the Large Hadron Collider (LHC) [18–21]. This came as a surprise, because  
 203 their presence in A+A collisions was typically associated with the collective expansion of the QGP. Similar correlations  
 204 were found in  $d+\text{Au}$  collisions at RHIC [22]. These findings have profound consequences for the interpretation of  $p+A$   
 205 collisions as a benchmark for cold-nuclear-matter effects and suggest that QGP could be produced in these systems.

206 The PHENIX experiment has used the versatility of RHIC, which allows for collisions of light nuclei, such as  $p$ ,  $d$ ,  
 207 and  ${}^3\text{He}$ , with larger nuclei, for systematic studies of particle correlations in small systems. In all systems studied,  
 208 high multiplicity events show large azimuthal anisotropies, measured as  $v_2$  and  $v_3$ , that can be related to the initial  
 209 geometry of the collision system and the build-up of collective behavior of the produced particles [23–27], which would  
 210 be indicative of QGP formation. This can also be seen at LHC energies where a measurement from  $p+\text{Pb}$  collisions [28]  
 211 shows  $v_2$  extending out past 20 GeV/ $c$  in  $p_T$ . These large azimuthal anisotropies also suggest the presence of radial  
 212 flow in a hydrodynamic expansion, which would have an effect on the yield below a few GeV/ $c$ .

213 Results from long range correlations have prompted great interest in finding other evidence of the possible formation  
 214 of QGP in small systems, such as parton energy loss or thermal photon emission. In such studies, data sets are typically  
 215 divided into ‘‘centrality classes’’ according to the particle multiplicity measured at forward rapidity on the side of  
 216 the outgoing larger nucleus [29]. Indeed, in  $p+\text{Pb}$  collisions at the LHC [30] and  $d+\text{Au}$  collisions at RHIC [31],  
 217 a suppression of the jet yield at high  $p_T$  was found for central collisions. However, the same analyses show a  
 218 significant enhancement of the jet yield in peripheral collisions, putting in question if the observed suppression is due  
 219 to energy loss [32] or whether there are other mechanisms at play, for example,  $x$ -dependent color fluctuation effects  
 220 in protons [33, 34] or biases in the centrality selection due to energy conservation [35].

221 In this paper new data on the system size and centrality dependence of  $\pi^0$  production are presented over a wide  
 222  $p_T$  range from 1 to 20 GeV/ $c$  from  $p+\text{Al}$ ,  $p+\text{Au}$ ,  $d+\text{Au}$ , and  ${}^3\text{He}+\text{Au}$  collisions at  $\sqrt{s_{NN}} = 200$  GeV compared to  
 223  $p+p$  collisions at the same energy. The data samples were recorded by the PHENIX experiment at RHIC during 2008  
 224 ( $p+p$  5.2 pb $^{-1}$ ,  $d+\text{Au}$  80 nb $^{-1}$ ), 2014 ( ${}^3\text{He}+\text{Au}$  24 nb $^{-1}$ ), and 2015 ( $p+p$  60 pb $^{-1}$ ,  $p+\text{Al}$  0.5 pb $^{-1}$ ,  $p+\text{Au}$  0.2 pb $^{-1}$ ).  
 225 The new  $p+p$  data are combined with the published results from  $p+p$  data taking in 2005 [36].

\* Deceased

† PHENIX Spokesperson: akiba@rcf.rhic.bnl.gov

## II. EXPERIMENTAL SETUP

To reconstruct the  $\pi^0$  meson, the electromagnetic calorimeter (EMCal) in the central arms of the PHENIX detector is used. The EMCal is segmented into eight sectors, four in the west and four in the east arm of the PHENIX experiment. The sectors in each arm cover 90 degrees in azimuth and  $\pm 0.35$  in pseudorapidity. All sectors in the west and the two top sectors in the east arm are made of 2,592 lead-scintillator (PbSc) towers each. The other two sectors comprise lead-glass crystals. For the analyses presented here only the PbSc sectors were used. At a distance of 5 meters from the nominal interaction point the angular segmentation of the PbSc sectors is  $\Delta\phi \times \Delta\eta \approx 0.01 \times 0.01$ . The energy resolution achieved is  $\delta E/E \approx 2.1\% \oplus 8.3\%/\sqrt{E[\text{GeV}]}$  and arrival times of clusters are recorded with a resolution of  $\approx 0.5$  ns. Further details can be found in Ref. [37].

For event selection and for centrality characterization the beam-beam counters (BBCs) are used, one on the north and one on the south side of the central arms. For asymmetric collision systems, the smaller (projectile) nucleus travels towards the north side and the larger (target) nucleus travels towards the south side. Each BBC is comprised of 64 Čerenkov counter modules. The BBCs are located at  $\pm 1.44$  m from the interaction point and cover a pseudorapidity range of  $3.0 < |\eta| < 3.9$ . The BBC modules have a timing resolution of  $\approx 0.1$  ns.

While the EMCal and the BBC were identical for data taking in 2008, 2014, and 2015, but there were new or modified detector components in each year. The most notable change was a silicon-vertex tracker (VTX) installed in the central-arm acceptance in 2011. Although the VTX and other new components are not used in this analysis, the effect on the material budget needs to be taken into account in the Geant3 [38] simulation used to calculate efficiency and acceptance corrections for each data set.

## III. DATA SAMPLES

Several data samples were taken with different trigger conditions for each of the collision systems. The minimum-bias (MB) data samples require coincidental hits in each of the two BBCs. For the data recorded in 2014 and 2015 the event vertex was required to be within  $\pm 10$  cm of the nominal  $z=0$  position. For the data recorded in 2008 the requirement was  $\pm 30$  cm.

The collected MB data samples correspond to  $\approx 88\%$  of the inelastic cross section for  $d+\text{Au}$  and  $^3\text{He}+\text{Au}$ , 84% for  $p+\text{Au}$ , 72% for  $p+\text{Al}$ , and 54% for  $p+p$ . The events that are not recorded by the MB trigger involve mostly single diffractive (SD) nucleon-nucleon collisions, which predominantly produce particles at forward or backward rapidity and thus do not lead to coincident hits in both BBCs. As the number of binary nucleon-nucleon collisions ( $N_{\text{coll}}$ ) increases from  $p+p$  to  $^3\text{He}+\text{Au}$  collisions, the effect of an individual SD nucleon-nucleon collision is averaged out and a larger fraction of the inelastic cross section is captured by the MB trigger.

All MB data samples in the analysis, except for the  $p+p$  samples, are subdivided into four centrality classes using the charge measured in the south BBC. The selections are 0%–20%, 20%–40%, 40%–60%, and the remainder of the MB sample (>60%). Here the percentage refers to the fraction of events relative to all inelastic collisions.

The high luminosity provided by RHIC enables the increase of the statistics at high  $p_T$ , beyond what the data acquisition bandwidth would allow using an MB trigger only, by taking data samples with a high energy threshold photon trigger, which PHENIX calls the ERT trigger. This trigger requires a minimum energy recorded in the EMCal segments (4x4 towers grouped to trigger tiles). Three different energy thresholds were used for each collision system. The ERT trigger thresholds are summarized in Table I. No coincidence in the BBC was required. These samples are again divided into the same centrality classes as the MB sample.

TABLE I. ERT trigger thresholds (GeV) for each collision system.

	$p+p$	$p+\text{Al}$	$p+\text{Au}$	$d+\text{Au}$	$^3\text{He}+\text{Au}$
ERTA	2.1	2.8	2.8	2.8	3.5
ERTB	2.8	3.5	3.5	3.5	4.0
ERTC	1.4	2.1	2.1	2.1	2.8

During the  $^3\text{He}+\text{Au}$ ,  $p+\text{Au}$ , and  $p+\text{Al}$  data collection samples were also taken with a high multiplicity trigger. This trigger required, in addition to the BBC coincidence, a larger minimum charge in the south BBC, which corresponds to a larger number of fired BBC modules. The threshold was set to 25, 35, and 48 BBC modules, for  $p+\text{Al}$ ,  $p+\text{Au}$ , and  $^3\text{He}+\text{Au}$  respectively. The thresholds were chosen such that the data samples approximately correspond to the top 5% most central collisions for each system.

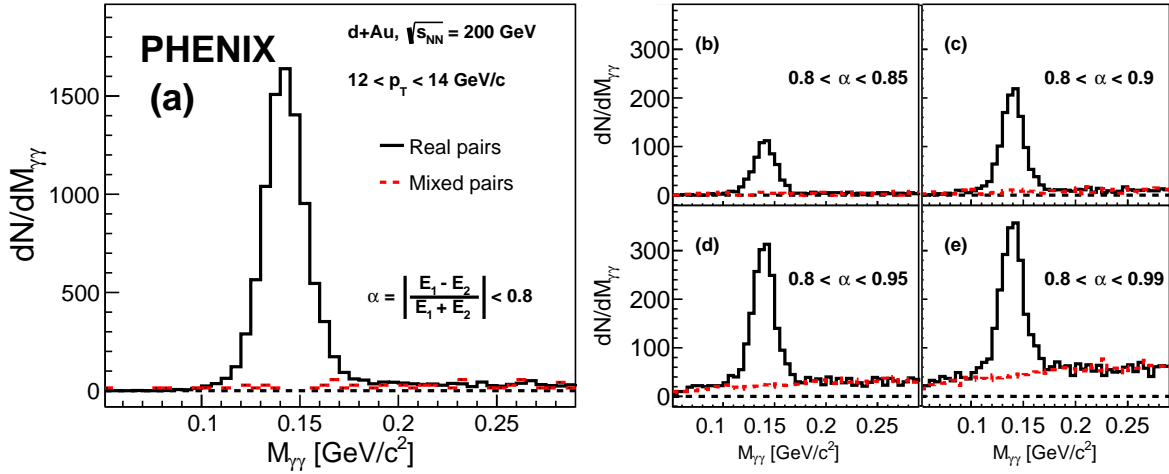


FIG. 1. (a) Invariant-mass example from  $d+Au$  collisions at  $12 < p_T < 14 \text{ GeV}/c$ . (b,c,d,e) The mass peak as a function of the asymmetry cut ( $\alpha$ ) on the two photons for the indicated  $\alpha$  ranges.

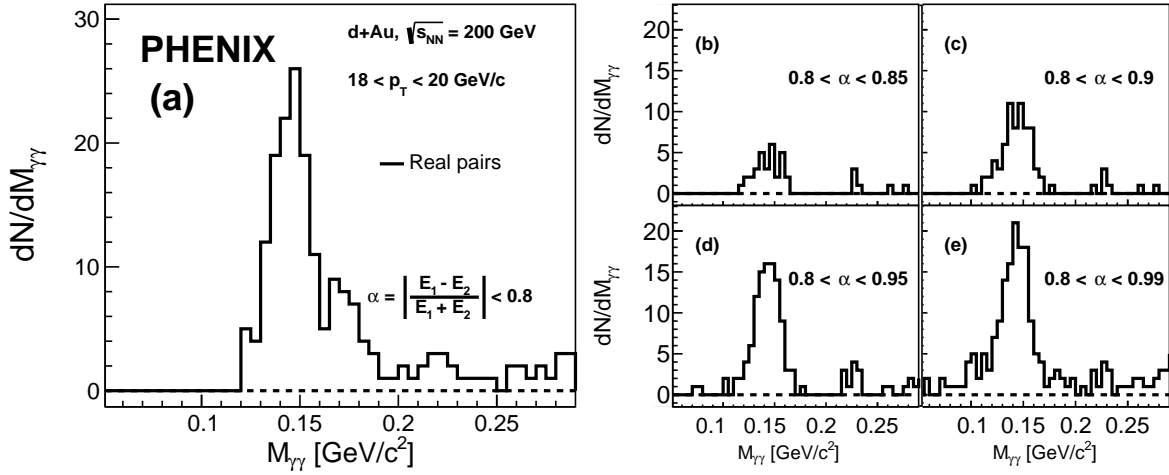


FIG. 2. (a) Invariant-mass example from  $d+Au$  collisions at  $18 < p_T < 20 \text{ GeV}/c$ . (b,c,d,e) The mass peak as a function of the asymmetry cut ( $\alpha$ ) on the two photons for the indicated  $\alpha$  ranges.

270

## IV. DATA ANALYSIS

271

### A. Yield measurement

272 Due to the high beam luminosity achieved at RHIC since 2010, PHENIX has recorded an increased number of  
 273 double interactions that are largest for the  $p+p$  data taken in 2015 and are noticeable for  $p+Au$  and  $p+Al$  data taken  
 274 the same year. The effect is negligible for the  $p+p$ ,  $d+Au$ , and  $^3\text{He}+Au$  data taken in 2008 and 2014, respectively.  
 275 For the 2015 data, double interactions were reduced by making cuts on the time of flight measured for towers in the  
 276 EMCal and the BBC modules. The cut on the EMCal requires the tower time to be within  $\pm 5 \text{ ns}$  of the expected  
 277 arrival time. This eliminates towers that are from different beam crossings. The BBC timing cut is used to reduce  
 278 pile-up collisions that happen during the same bunch crossing. Such events are identified by large deviations of the  
 279 time measured for individual BBC modules from the event average. For data from 2014 and 2008 no cuts were applied.  
 280 Any residual pileup events are accounted for in the systematic uncertainties.

281 The reconstruction of neutral pions is performed via the  $\pi^0 \rightarrow \gamma\gamma$  decay channel. The methods used by PHENIX  
 282 have been described extensively in Ref. [39] and will only be summarized in this paper. As a first step, neighboring

PbSc towers with energy deposits above 0.015 GeV are grouped into clusters. All clusters within one sector that have an energy of at least 0.3 GeV are combined into pairs. A minimum distance of 8 cm between the two cluster centers is required, corresponding to  $\approx 1.5$  tower separation between clusters. For each remaining pair, the invariant mass ( $M_{\gamma\gamma}$ ) and  $p_T$  are calculated. Invariant-mass distributions are generated in bins of  $p_T$  and collision centrality. All mass distributions show a clear peak at the  $\pi^0$  mass and a combinatorial background that is largest at events with low  $p_T$  and in central collisions.

To extract the  $\pi^0$  yield, the background in the  $\pi^0$  peak region needs to be subtracted. For  $p_T$  below 12 GeV/ $c$  an asymmetry cut of  $\alpha < 0.8$  is applied to reduce the combinatorial background. Here the asymmetry is defined as  $\alpha = \left| \frac{(E_1 - E_2)}{(E_1 + E_2)} \right|$ , where  $E_1$  and  $E_2$  are the energies of the two photon clusters. For  $p_T$  above 12 GeV/ $c$  the cut is relaxed to  $\alpha < 0.95$  as discussed below.

The bulk of the background is estimated and subtracted by an event mixing technique that combines clusters from different events with similar vertex position ( $z_{\text{vtx}}$ ) and centrality. The shape of the mass distributions obtained from mixed events does not perfectly describe the combinatorial background in data. The mismatch results from correlated clusters in the event that are not accounted for in the mixed event technique.

For the MB samples, the mismatch is small and a two-step procedure is used for the subtraction. First, the mass distribution from mixed events is normalized in the mass region below and above the  $\pi^0$  peak,  $0.05 < M_{\gamma\gamma} < 0.1$  GeV/ $c^2$  and  $0.2 < M_{\gamma\gamma} < 0.4$  GeV/ $c^2$ , respectively. After subtracting the normalized distributions from all bins, a residual background remains. This is approximated by a line that is fitted to the same mass regions around the  $\pi^0$  peak and then also subtracted.

For the ERT data samples, the shape difference is more significant and thus a different approach is used. Instead of normalizing the mixed event distribution with a constant, the ratio of data/mixed events is fit with a second-order polynomial in the window around the  $\pi^0$  peak. This function is then used to normalize the mixed event distributions bin-by-bin, in the same mass intervals below and above the mass peak as in the MB samples (see above). No residual background subtraction is needed in this case.

At very high- $p_T$ , typically larger than 15 GeV/ $c$ , the combinatorial background is so small that neither normalization strategy for the mixed events gives stable results. Instead, the average count per mass bin, determined in the region below and above the  $\pi^0$  peak, is subtracted.

After the background subtraction, yields of  $\pi^0$  are calculated from the mass spectra by counting the entries within  $2\sigma$  of the peak, where the  $\sigma$  is set by fitting the counts in the  $\pi^0$  region to a Gaussian.

Above 12 GeV/ $c$ , the two photon clusters from the  $\pi^0$  meson begin to overlap more and frequently merge into a single cluster. The asymmetry cut at  $\alpha < 0.8$ , which was used to reduce the combinatorial background, starts to limit the  $\pi^0$  reconstruction efficiency and with it the effective  $p_T$  reach of the measurement. Because the combinatorial background is rather small at high  $p_T$ , the asymmetry cut can be relaxed to increase the reconstruction efficiency. Figures 1 and 2 show mass distributions from  $d$ +Au collisions in the  $p_T = 12$  to 14 GeV/ $c$  and 18 to 20 GeV/ $c$  bins with different asymmetry cuts. The additional statistics recovered by extending the asymmetry cuts are clearly visible. In particular, in the higher  $p_T$  bin, increasing the cut from  $\alpha < 0.8$  to  $< 0.95$  effectively increases the statistics. Because it is also evident that the background increases, the looser cut is only used above  $p_T > 12$  GeV/ $c$ . The background subtraction and  $\pi^0$  yield calculation follow the same steps as outlined above for lower  $p_T$ . The background estimate from event mixing is also shown on Fig. 1. In Fig. 2, the background is estimated from the average bin content around the  $\pi^0$  peak.

## B. Trigger selection

At this stage of the analysis, raw  $\pi^0$  yields are available for all data samples in different bins of  $p_T$  and centrality. Figure 3(a) compares the raw yields from the MB and ERT samples in  $p$ + $p$  collisions from the 2015 data set. Figure 3(b) shows the ratio of individual samples to a common fit. The ERT trigger turn on curves are clearly visible.

In the next step the raw yields from the MB and ERT trigger samples are combined for a given collision system and centrality. First, the ERT trigger samples are corrected for the trigger efficiency, which is calculated as a function of the  $\pi^0$   $p_T$ . The trigger efficiency has a smooth turn on around the trigger energy threshold and plateaus near 100% at higher  $p_T$ . A data driven method is used that compares the ERTC to the MB sample and the ERTA/ERTB to the ERTC sample to establish the turn on curve of the different trigger thresholds. The corrected spectra agree very well in the range where the trigger efficiency is larger than 30%.

To assure the largest statistical accuracy in each  $p_T$  bin, the MB triggered events are used in the low- $p_T$  region, the ERTC trigger in the mid- $p_T$  region, and the ERTB trigger at high- $p_T$ . These transitions happen at different  $p_T$  thresholds for different collision systems. The  $p_T$  thresholds are set near the point where the trigger efficiency reaches its plateau value, typically close to twice the trigger threshold shown in Table I. The ERTA triggered samples are

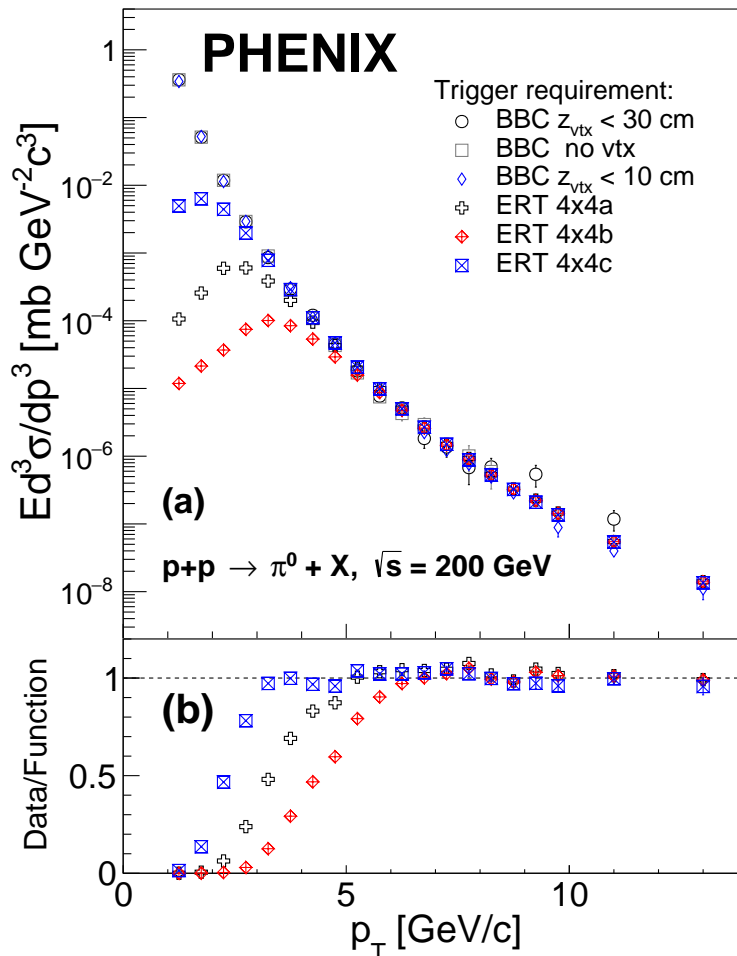


FIG. 3. (a) Invariant yield example from 2015  $p+p$  collisions using different hardware trigger configurations. (b) The ratio of the different high- $p_T$  triggers to a common Tsallis fit for all different triggers.

337 used to crosscheck the results.

338

### C. Corrections to the yield

339 Next, the raw  $p_T$  spectra need to be corrected for distortions due to the finite detector acceptance and overall  
 340 detection efficiency (including detector effects and analysis cuts). These are determined simultaneously as one single  
 341 correction as a function of  $p_T$  using a full Geant3 Monte Carlo (MC) simulation of the PHENIX detector setup. They  
 342 are commonly referred to as acceptance-efficiency corrections (see Fig 4), which are determined separately for each  
 343 centrality selection to account for any multiplicity dependent effects. For each running period, a separate simulation  
 344 setup is used that describes the PHENIX detector configuration specific to that period. Samples of single  $\pi^0$  meson  
 345 are simulated with a flat  $p_T$  distribution from 0 to 30 GeV/c, full azimuthal coverage, and in one unit of rapidity at  
 346 midrapidity. The resulting simulated detector responses are embedded into real data from the same running period  
 347 and reconstructed using the same analysis methods applied to the data. The simulation was tuned so that  $\pi^0$  peak  
 348 positions and widths reconstructed from the simulation matched the experimental data. Each reconstructed  $\pi^0$  is  
 349 weighted with a realistic production probability for the  $p_T$  of the input  $\pi^0$ . Because the true production probability  
 350 is unknown, the weighting needs to be iterated. The probability is multiplied by the ratio of the measured raw  
 351  $\pi^0$  distribution over the reconstructed  $\pi^0$  distribution from the simulation. The modified probability is then used  
 352 as the new weight. The process is iterated until convergence, which typically requires only a few steps. The final  
 353 acceptance-efficiency corrections are calculated as the ratio of the reconstructed number of  $\pi^0$  at a given  $p_T$  over the

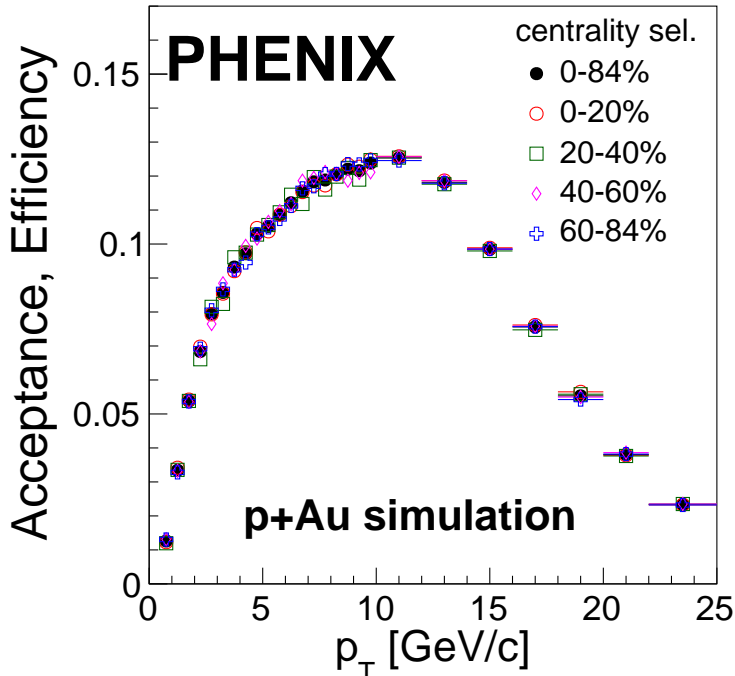


FIG. 4. The MC result of the acceptance and efficiency in  $p+Au$  collisions with the selected centrality classes as indicated.

354 number of generated ones at that  $p_T$  in one unit of pseudorapidity at midrapidity and  $2\pi$  in azimuth.

355 Additionally, the yield in each centrality selection for a given collision system must be corrected for the bias towards  
 356 higher event multiplicity, and hence more central events, for nondiffractive nucleon-nucleon collisions compared to  
 357 diffractive collision events with the same impact parameter (see [29] for full details). The bias factor  $f_{\text{bias}}$ , which is used  
 358 to scale the  $p_T$  spectra, is calculated using a Glauber Model MC calculation [41] in conjunction with the assumption of  
 359 a negative-binomial multiplicity distribution of particles produced in individual nucleon-nucleon collisions. The same  
 360 Glauber calculation is used to characterize each centrality class by the number of binary nucleon-nucleon collisions  
 361  $N_{\text{coll}}$ , number of nucleon participants  $N_{\text{part}}$ , and other relevant properties related to the collision geometry, such as  
 362  $N_{\text{proj}}$ , the number of participants in the projectile nucleus. For MB collisions, the  $f_{\text{bias}}$  also includes the extrapolation  
 363 from the recorded cross section to the full inelastic cross section (0%–100% centrality). The average values of  $N_{\text{coll}}$ ,  
 364  $N_{\text{part}}$ ,  $N_{\text{proj}}$ , and the bias factor  $f_{\text{bias}}$  are given in Table II.

## 365 V. SYSTEMATIC UNCERTAINTY

366 There are many sources of systematic uncertainty that need to be evaluated. They are separated into two groups:  
 367 (i) uncertainty on the event characterization and (ii) uncertainty on the  $\pi^0$  yield extraction.

368 The event characterization is done using Glauber model simulations and the uncertainties were determined by  
 369 varying the input to the Glauber model and various assumptions used in [29]. The results are included in Table II.  
 370 The quantities calculated from the Glauber model simulation are highly correlated. For example, any change in the  
 371 assumed nucleon-nucleon cross section will lead to a simultaneous change of  $N_{\text{coll}}$ ,  $N_{\text{part}}$ , and  $N_{\text{proj}}$ . Thus, in ratios  
 372 such as  $N_{\text{coll}}/N_{\text{proj}}$ , some of the systematic uncertainties cancel. This was taken into account in the errors quoted in  
 373 Table III.

374 The uncertainties on the  $\pi^0$  invariant yield are summarized in Table III for the different running periods. The total  
 375 uncertainty on the  $\pi^0$  invariant yield varies between 8%–10% for  $p_T$  below 8 GeV/ $c$  and increases to nearly 15% at 20  
 376 GeV/ $c$ . They have little dependence on collision systems or centrality selection. The uncertainties on the  $\pi^0$  invariant  
 377 yield were obtained with similar methods for all data sets. They are highly correlated within a running period and  
 378 somewhat correlated between running periods. In particular, the uncertainty on the energy scale and the uncertainty  
 379 due to shower merging are correlated between all data sets. In 2014 and 2015, the experimental setup was nearly  
 380 identical and therefore the acceptance-efficiency correction, losses due to photon conversions, and uncertainties due

TABLE II. Summary of the  $N_{\text{coll}}$ ,  $N_{\text{part}}$ ,  $N_{\text{proj}}$ ,  $f_{\text{bias}}$  calculated using a Glauber MC simulation [29, 40]. The ratio  $N_{\text{coll}}/N_{\text{proj}}$  is also quoted for  $d$  and  ${}^3\text{He}$  projectiles, because some systematic uncertainties cancel in this ratio. The last column is the measured charged particle multiplicity ( $dN_{\text{ch}}/d\eta$ ) in the midrapidity region [40].

system	centrality	$\langle N_{\text{coll}} \rangle$	$\langle N_{\text{part}} \rangle$	$\langle N_{\text{proj}} \rangle$	$f_{\text{bias}}$	$\langle N_{\text{coll}} \rangle / \langle N_{\text{proj}} \rangle$	$dN_{\text{ch}}/d\eta$
$p+p$		1	2	1	$0.73 \pm 0.07$	-	$2.38 \pm 0.09$
$p+\text{Al}$	0%–5%	$4.1 \pm 0.3$	$4.5 \pm 0.3$	1	$0.81 \pm 0.01$	-	$5.5 \pm 0.8$
	0%–20%	$3.4 \pm 0.3$	$4.4 \pm 0.3$	1	$0.81 \pm 0.01$	-	$5.1 \pm 0.7$
	20%–40%	$2.3 \pm 0.1$	$3.3 \pm 0.1$	1	$0.90 \pm 0.02$	-	$4.0 \pm 0.6$
	40%–60%	$1.8 \pm 0.1$	$2.8 \pm 0.2$	1	$0.99 \pm 0.03$	-	$3.3 \pm 0.3$
	60%–72%	$1.3 \pm 0.1$	$2.3 \pm 0.2$	1	$1.15 \pm 0.06$	-	$2.7 \pm 0.1$
	0%–100%	$2.1 \pm 0.1$	$3.1 \pm 0.1$	1	$0.80 \pm 0.02$	-	$4.0 \pm 0.5$
$p+\text{Au}$	0%–5%	$9.7 \pm 0.6$	$10.7 \pm 0.6$	1	$0.86 \pm 0.01$	-	$12.3 \pm 1.7$
	0%–20%	$8.2 \pm 0.5$	$9.2 \pm 0.5$	1	$0.90 \pm 0.01$	-	$10.4 \pm 1.5$
	20%–40%	$6.1 \pm 0.4$	$7.1 \pm 0.4$	1	$0.98 \pm 0.01$	-	$7.7 \pm 1.1$
	40%–60%	$4.4 \pm 0.3$	$5.4 \pm 0.3$	1	$1.02 \pm 0.01$	-	$5.7 \pm 0.8$
	60%–84%	$2.6 \pm 0.2$	$3.6 \pm 0.2$	1	$1.00 \pm 0.06$	-	$3.5 \pm 0.5$
	0%–100%	$4.7 \pm 0.3$	$5.7 \pm 0.3$	1	$0.858 \pm 0.014$	-	$6.7 \pm 0.9$
$d+\text{Au}$	0%–5%	$18.1 \pm 1.2$	$17.8 \pm 1.2$	$1.97 \pm 0.02$	$0.91 \pm 0.01$	$8.98 \pm 0.59$	$18.9 \pm 1.4$
	0%–20%	$15.1 \pm 1.0$	$15.2 \pm 0.6$	$1.95 \pm 0.01$	$0.94 \pm 0.01$	$7.46 \pm 0.50$	$16.4 \pm 1.2$
	20%–40%	$10.2 \pm 0.7$	$11.1 \pm 0.6$	$1.84 \pm 0.01$	$1.00 \pm 0.01$	$5.71 \pm 0.39$	$12.2 \pm 0.9$
	40%–60%	$6.6 \pm 0.4$	$7.8 \pm 0.4$	$1.65 \pm 0.02$	$1.03 \pm 0.02$	$4.16 \pm 0.28$	$8.7 \pm 0.6$
	60%–88%	$3.2 \pm 0.2$	$4.3 \pm 0.2$	$1.36 \pm 0.02$	$1.03 \pm 0.06$	$2.27 \pm 0.15$	$4.1 \pm 0.3$
	0%–100%	$7.6 \pm 0.4$	$8.6 \pm 0.4$	$1.62 \pm 0.01$	$0.889 \pm 0.003$	$4.35 \pm 0.24$	$9.5 \pm 1.0$
${}^3\text{He}+\text{Au}$	0%–5%	$26.1 \pm 2.0$	$25.0 \pm 1.6$	$2.99 \pm 0.01$	$0.92 \pm 0.01$	$8.72 \pm 0.64$	$23.6 \pm 2.6$
	0%–20%	$22.3 \pm 1.7$	$21.8 \pm 1.3$	$2.95 \pm 0.01$	$0.95 \pm 0.01$	$7.30 \pm 0.52$	$21.4 \pm 2.3$
	20%–40%	$14.8 \pm 1.1$	$15.4 \pm 0.9$	$2.75 \pm 0.03$	$1.01 \pm 0.01$	$5.41 \pm 0.37$	$16.1 \pm 1.8$
	40%–60%	$8.4 \pm 0.6$	$9.5 \pm 0.6$	$2.29 \pm 0.04$	$1.02 \pm 0.01$	$3.85 \pm 0.25$	$10.3 \pm 1.1$
	60%–88%	$3.4 \pm 0.3$	$4.6 \pm 0.3$	$1.56 \pm 0.05$	$1.03 \pm 0.05$	$2.05 \pm 0.12$	$4.4 \pm 0.5$
	0%–100%	$10.4 \pm 0.7$	$11.4 \pm 0.5$	$2.22 \pm 0.02$	$0.89 \pm 0.01$	$4.13 \pm 0.24$	$12.2 \pm 1.4$

381 to off-vertex decays are also correlated for data sets taken during those years. For data sets taken within the same  
382 running period, all systematic uncertainties, except for the  $\pi^0$  peak extraction and the effect of double interactions, are  
383 correlated. The correlations of the systematic uncertainties have been taken into account when combining data sets  
384 or calculating ratios of data sets by determining the full error matrix and using the Best Linear Unbiased Estimate  
385 (BLUE) algorithm [42–44] to calculate the weight for each  $p_T$  and each measurement.

386 The remainder of this section provides more details on the evaluation of the systematic uncertainties on the  $\pi^0$   
387 yield determination, which is split into the extraction of the raw  $\pi^0$  yield and the corrections that need to be applied  
388 to it.

### 389 A. Raw $\pi^0$ yield extraction

390 The raw  $\pi^0$  yield is extracted from an invariant mass  $M_{\gamma\gamma}$  distribution, which involves the subtraction of a back-  
391 ground distribution below a  $\pi^0$  peak. Except for at very high  $p_T$ , this is done using the mixed event technique. This  
392 subtraction is typically accurate to better than 4%. In general, the uncertainties on the background subtraction are  
393 determined by changing the assumption on the shape of the background and how it is normalized. Many different  
394 strategies can be used, as they all give similar results. Here, one example is given, the strategy that was used for  
395 the 2015 MB data sets, which were used to extract the  $\pi^0$  yield at lower  $p_T$  values for  $p+\text{Au}$ ,  $p+\text{Al}$ , and  $p+p$ . The

TABLE III. Summary of systematic uncertainties on the  $\pi^0$  invariant yields from different running periods.

Systematic uncer. $p_T$ [GeV/c]	2015 $p+Au$ , $p+Al$ , $p+p$			2014 $^3\text{He}+Au$			2008 $d+Au$ , $p+p$		
	2	8	20	2	8	20	2	8	20
Peak Extraction	4.4%	3.4%	1%	2.7%	4.1%	2%	4.8%	2.9%	1.5%
Energy Scale	3.8%	6.5%	7.1%	3.0%	5.2%	5.7%	4.6%	7.9%	8.7%
Acceptance-Efficiency	3%	2.5%	1%	4%	4%	4%	3%	2.5%	1%
Cluster Merging	<0.1%	<0.1%	9.0%	<0.1%	<0.1%	12%	<0.1%	<0.1%	10%
Conversion Loss	5%	5%	5%	5%	5%	5%	2.5%	2.5%	2.5%
Double Interactions	4%	3%	4%	<1%	<1%	<1%	1%	2.5%	4%
Off Vertex Decays	3%	3%	3%	3%	3%	3%	3%	3%	3%
Total	9.6%	10.1%	13.0%	8.3%	9.8%	14.1%	8.3%	10.0%	14.5%

normalization of the mixed event background is determined in different ranges below and above the  $\pi^0$  peak. For any normalization, after the mixed event subtraction there is a residual background, which is then fitted. For each normalization the fit range is varied to extract the residual background via a first-order polynomial. Then in each case the window for the  $\pi^0$  yield extraction is varied from 1 to 3 sigma around the  $\pi^0$  peak. The variation of the resulting  $\pi^0$  yields, after correcting for the different  $\sigma$  ranges, is used to estimate the systematic uncertainty.

The accuracy with which the  $\pi^0$  yield can be extracted depends on the amount of background. In general, the smaller the particle multiplicity in the event and/or the larger the  $\pi^0$   $p_T$ , the smaller the background. However, the accuracy with which the background can be determined for a particular  $p_T$  and centrality bin is driven by the available statistics. The dominant effect changes depending on the  $\pi^0$   $p_T$  and the MB or ERT data set.

## B. Corrections of the raw yield

The acceptance-efficiency correction accounts for all distortions to the  $\pi^0$  spectra that can be evaluated with the detailed simulation of  $\pi^0$  measurements in the PHENIX experiment. The accuracy of the simulation determines the size of systematic uncertainties. Accordingly, the simulation output was carefully compared to the data.

These distortions include, besides the actual corrections for detector acceptance and  $\pi^0$  reconstruction, the one for the energy scale and resolution, merging of clusters, and losses due to photon conversions. While the corrections were determined simultaneously, possible uncertainties are studied separately. In Table III these are identified as “Acceptance-Efficiency”, “Energy Scale”, “Cluster Merging”, and “Conversion Loss”, respectively.

The energy scale and resolution was tuned by matching the  $\pi^0$  peak position and width in simulation and data, as function of  $p_T$ , to a better than 0.5%–1% agreement, depending on the data set. The uncertainty is then determined by varying the energy scale and resolution within the achieved accuracy. The  $\pi^0$  yields change by less than 4%–5% at 2 GeV/c and up to 7%–9% at 20 GeV/c.

To study the accuracy of the reconstruction efficiency correction, cuts applied in the  $\pi^0$  reconstruction were varied and the analysis was repeated. The changes in the  $\pi^0$  yield were used to set the systematic uncertainties. They are typically smaller than 4%, but may be limited by statistical uncertainties. The uncertainty on the acceptance was determined from the precision of the survey of the EMCal. It is negligible compared to the uncertainties on the reconstruction efficiency.

Because the two decay photons from the decay of a high  $p_T$   $\pi^0$  are strongly boosted along the  $\pi^0$  direction, the average opening angle becomes small, resulting in only a small separation between the impact points on the surface of the EMCal. At  $\approx 10$  GeV/c, the two clusters start to merge. Initially, this happens only for very symmetric decays characterized by a small energy asymmetry ( $\alpha$ ). With increasing  $p_T$ , more and more clusters merge, leading to a systematic decrease in reconstruction efficiency towards higher  $p_T$ . The accuracy with which the MC simulation reproduces the cluster merging is verified by reconstructing  $\pi^0$  mesons from three exclusive asymmetry bins: 0–0.4, 0.4–0.8, and 0.8–0.95. After fully correcting the  $\pi^0$  yields, the results are compared and the differences are used to estimate the systematic uncertainty. It reaches  $\approx 10\%$  towards the end of the kinematic reach of the measurement.

Some photons convert into  $e^+e^-$  pairs before they reach the EMCal. If the radial location of the conversion point is close to the EMCal, outside the magnetic field, the  $e^+$  and  $e^-$  will hit the EMCal in close proximity, resulting in one cluster with the full energy of the converted photon. In that case, it is likely that the  $\pi^0$  is reconstructed. However, if the conversion point is closer to the vertex, and in the magnetic field, the  $\pi^0$  will not be reconstructed, because the

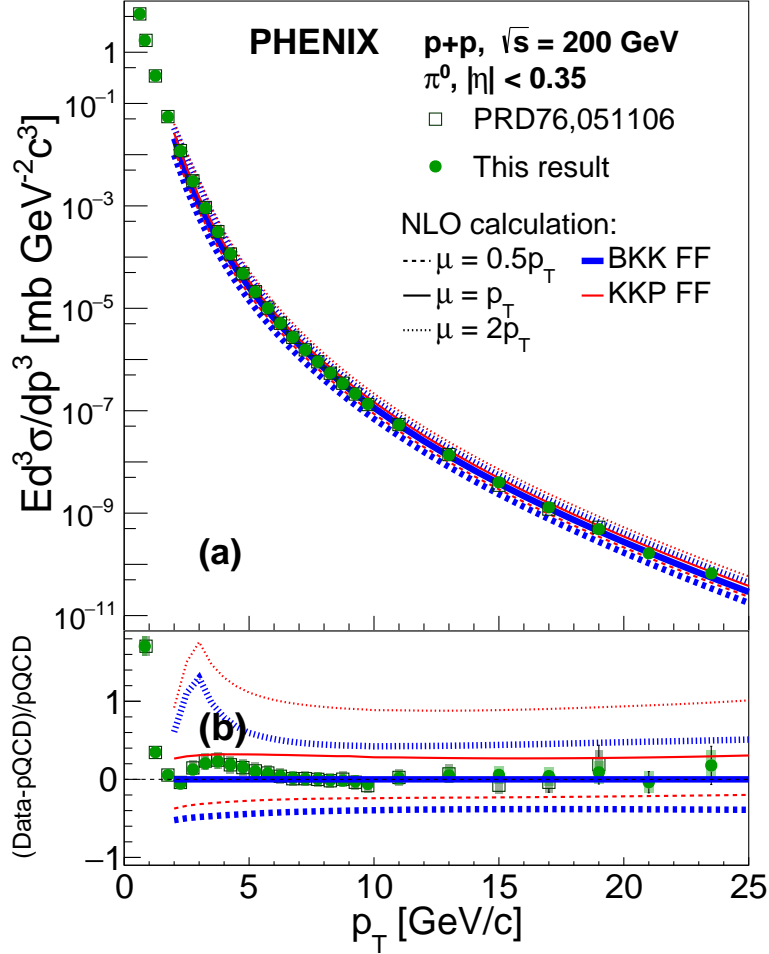


FIG. 5. (a) Differential cross section of  $\pi^0$  in  $p+p$  collisions at  $\sqrt{s} = 200$  GeV. The data are compared with the indicated pQCD calculations. (b) The ratio of the data points to the NLO calculation with BKK and a scale of  $\mu = p_T$ .

434 electron tracks bend in opposite directions, depositing their energy in two separate clusters.

435 Prior to 2010, before the VTX was installed,  $\approx 10\%$  of the  $\pi^0$  were not reconstructed because one of the photons  
 436 converted in the detector material. Due to the additional material of the VTX detector close to the vertex, this  
 437 number increases to  $\approx 24\%$ . The accuracy with which the loss can be determined depends solely on the accuracy with  
 438 which the material budget is known and implemented in the Geant3 simulation. The resulting uncertainties on the  
 439  $\pi^0$  yield are 2.5% and 5%, before and after installation of the VTX. There is no significant momentum dependence.

440 All data sets from 2015 ( $p+p$ ,  $p+Al$ , and  $p+Au$ ) were taken at high instantaneous luminosity, resulting in a  
 441 significant number of recorded double interactions. These were actively identified and removed by timing cuts on  
 442 the EMCal and BBC. The effect of any remnant double interaction was estimated by splitting the data samples  
 443 into subsets taken at higher, medium, and lower luminosity. The analysis was repeated for each sample, and the  
 444  $\pi^0$  yields were found to be consistent within 3%–4%. This difference was assigned as a systematic uncertainty. For  
 445 the 2008 data sets ( $p+p$  and  $d+Au$ ), only the EMCal timing cuts were applied to remove pileup events. Here, the  
 446 possible contamination was estimated by the number of  $\pi^0$  for which at least one cluster had a time off by  $>5$  ns. The  
 447 contribution was 1% at high  $p_T$  and  $\approx 4\%$  at lower  $p_T$ . For the 2014  $^3\text{He}+Au$  data no sizable effect was found.

448 Finally, the uncertainty of the normalization of the data taken with the ERT trigger to the MB data is examined.  
 449 It is estimated from the uncertainty on the linear fit of the ratio between the ERT and MB data in the region where  
 450 the ERT trigger is fully efficient. This uncertainty is smaller than 1% and not listed in Table III.

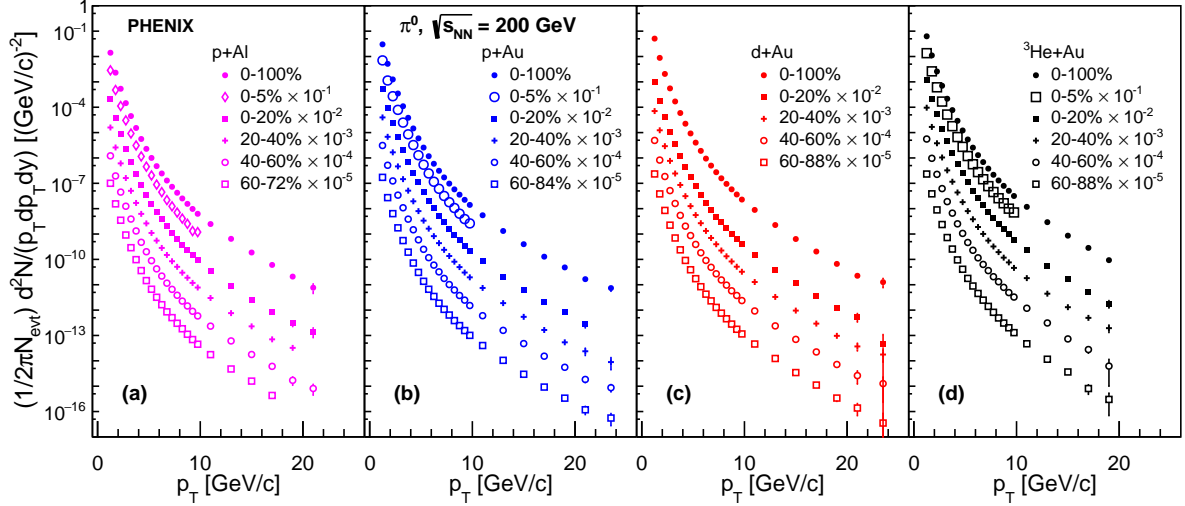


FIG. 6. Invariant yield of  $\pi^0$  from (a)  $p$ +Al, (b)  $p$ +Au, (c)  $d$ +Au, and (d)  ${}^3\text{He}$ +Au at  $\sqrt{s_{NN}} = 200$  GeV. For each collision system the yield is shown for the inelastic cross section and for different centrality selections 0%–20%, 20%–40%, 40%–60%, and larger than 60%. For  $p$ +Al,  $p$ +Au, and  ${}^3\text{He}$ +Au an additional 0%–5% centrality selection is shown, which was recorded using a dedicated high multiplicity trigger.

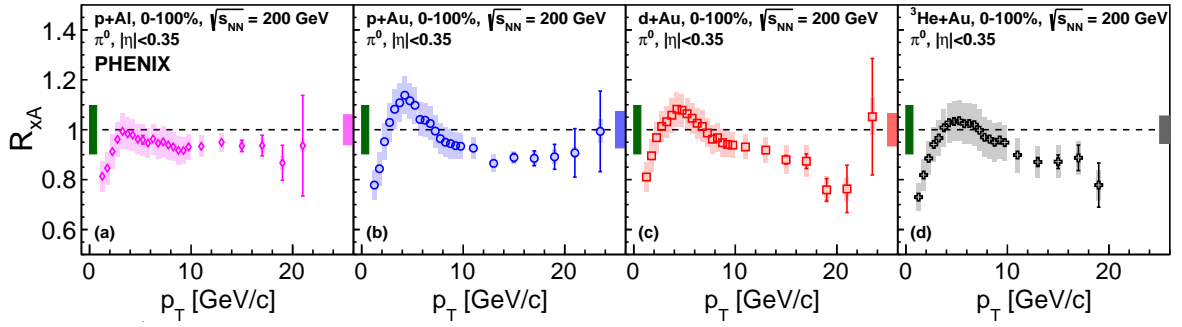


FIG. 7. Nuclear-modification factors from inelastic (a)  $p$ +Al, (b)  $p$ +Au, (c)  $d$ +Au, and (d)  ${}^3\text{He}$ +Au collisions at  $\sqrt{s_{NN}} = 200$  GeV. The error bars represent the statistical uncertainties, while the boxes represent the systematic uncertainties. The high- $p_T$  box in each panel is the  $N_{\text{coll}}$  uncertainty from the Glauber model, while the low- $p_T$  box represents the overall normalization uncertainty from  $p$ + $p$  collisions.

## VI. RESULTS AND DISCUSSION

### A. The $p$ + $p$ reference

PHENIX has previously published the  $\pi^0$   $p_T$  spectrum from  $p$ + $p$  collisions at  $\sqrt{s} = 200$  GeV [36] based on data taken in 2005 corresponding to  $3.4 \text{ pb}^{-1}$ . In 2008 and 2015 RHIC provided further  $p$ + $p$  collisions, increasing the integrated luminosity by  $5.2 \text{ pb}^{-1}$  and  $60 \text{ pb}^{-1}$  respectively.

With the increase in the data sample, the precision of the measurement was improved and extended to higher  $p_T$ . Because the detector configurations and the ERT trigger settings were different for the 2008 and 2015 data sets, the  $\pi^0$  spectra were measured separately. The results were combined with those from 2005.

The new and published measurements were made with the PHENIX EMCAL using the same analysis strategy, thus the  $\pi^0$  yield determinations have largely, but not completely, correlated systematic uncertainties. To combine the three data sets, the correlations between individual systematic uncertainties were studied and accounted for using the BLUE method [43]. In addition to the uncertainties due to the  $\pi^0$  reconstruction, there is an overall normalization uncertainty of 9.7% [36] that accounts for the limited accuracy with which the  $p$ + $p$  MB trigger efficiency (see Table II) is known. This uncertainty is common to all  $p$ + $p$  measurements.

Figure 5 compares the combined  $\pi^0$   $p_T$  spectrum from  $p$ + $p$  collisions (2005, 2008, 2015) to the earlier published

466 result. The combined result is in excellent agreement with data taken in 2005, but has significantly improved statistics  
 467 and extends the  $p_T$  range up to 25 GeV/ $c$ . The systematic uncertainties are slightly reduced with respect to those of  
 468 the 2005 data alone.

469 Also shown in Fig. 5 are next-to-leading-order (NLO) perturbative-quantum-chromodynamics (pQCD) calcula-  
 470 tions [45] with two different fragmentation functions (BKK and KKP) and for three different scales  $\mu = p_T/2$ ,  $p_T$ ,  
 471 and  $2p_T$ . For the calculations, the same CT14 free proton parton distribution function (PDF) was used and only the  
 472 fragmentation function in the same framework was changed. Within the assumed range of scales both fragmentation  
 473 functions are consistent with the data. BKK would require a scale of  $\mu = p_T$ , while KKP envelopes the data between  
 474  $\mu = p_T/2$  and  $p_T$  scales.

## 475 B. Small system $p_T$ spectra and nuclear-modification factor

476 To simplify the labeling and description of each variable, the same notation is used for each small system. The  
 477 “projectile” nucleus ( $p$ ,  $d$ , or  ${}^3\text{He}$ ) is denoted by  $x$  and the “target” nucleus (Au or Al) by  $A$ . This notation is used  
 478 in both the plots and text unless a specific system is being discussed.

### 479 1. $p_T$ spectra

480 Figure 6 presents  $\pi^0$   $p_T$  spectra from (a)  $p+\text{Al}$ , (b)  $p+\text{Au}$ , (c)  $d+\text{Au}$ , and (d)  ${}^3\text{He}+\text{Au}$ . The data are presented as  
 481 the invariant  $\pi^0$  yield per collision as a function of  $p_T$ . The 0%–100% range corresponds to the full inelastic cross  
 482 section. The other centrality ranges correspond to 0%–5%, 0%–20%, 20%–40%, 40%–60%, and above 60% measured  
 483 percentile of the events selected according to the multiplicity measured in the BBC on the south side (heavy nucleus  
 484 going side). Different centrality selections are scaled by factors 1/10 for visibility. The 0%–5% centrality selection,  
 485 which is available for  ${}^3\text{He}+\text{Au}$ ,  $p+\text{Au}$ , and  $p+\text{Al}$  collisions, was taken with a high multiplicity BBC trigger and has  
 486 a  $p_T$  range limited to below 10 GeV/ $c$ .

### 487 2. Nuclear-modification factor

488 For a quantitative comparison across systems and centrality selections the nuclear-modification factor ( $R_{xA}$ ) is  
 489 used. It is defined as:

$$R_{xA} = \frac{dN_{xA}/dp_T \times \sigma_{pp}^{\text{inel}}}{\langle N_{\text{coll}} \rangle \times d\sigma_{pp}/dp_T}, \quad (1)$$

490 where  $dN_{xA}/dp_T$  is the invariant yield per  $x+A$  collisions,  $d\sigma_{pp}/dp_T$  is the invariant cross section in  $p+p$  collisions,  
 491  $\sigma_{pp}^{\text{inel}} = 42\text{mb}$  is the inelastic  $p+p$  cross section, and  $\langle N_{\text{coll}} \rangle$  is the average number of binary nucleon-nucleon collisions  
 492 given in Table II. The  $\langle N_{\text{coll}} \rangle$  is obtained by the Glauber MC model [46] used in all PHENIX papers and the detailed  
 493 study of the model in smaller system centrality applications was described in [29]. A nuclear-modification factor of  
 494  $R_{xA} \approx 1$  at high  $p_T$  indicates that  $\pi^0$  production through hard scattering processes in  $x+A$  collisions is well described  
 495 by an incoherent superposition of  $p+p$  collisions.

### 496 3. $R_{xA}$ for inelastic collisions

497 The nuclear-modification factors,  $R_{xA}$ , for inclusive  $\pi^0$  production from inelastic  $p+\text{Al}$ ,  $p+\text{Au}$ ,  $d+\text{Au}$ , and  ${}^3\text{He}+\text{Au}$   
 498 collisions are shown in Fig. 7. They are calculated using the  $p+p$  reference from the combined 2005, 2008, and 2015  
 499 data. The correlations of the systematic uncertainties on the  $\pi^0$  reconstruction for different data sets are taken into  
 500 account using the BLUE method. The overall normalization uncertainties on  $p+p$  and on  $N_{\text{coll}}$  are shown separately  
 501 at the lowest and highest  $p_T$ , respectively.

502 Each data set exhibits the characteristic  $p_T$  dependence of the Cronin effect, an initial rise from below unity to  
 503 a peak around  $p_T$  of 4 GeV/ $c$ , followed by a drop and a leveling off at high  $p_T$ . The constant value at high  $p_T$  is  
 504 independent of the collision system at a value of  $R_{xA} \approx 0.9$ , which is consistent with unity within the systematic  
 505 uncertainties on the scale and  $N_{\text{coll}}$ . The fact that  $R_{xA}$  at high  $p_T$  is consistent with unity and that there is no system  
 506 size dependence suggest that there is little to no modification of the hard scattering component in small systems.

507 To investigate any possible system size dependence of the modification at lower  $p_T$ , the ratio of the maximum of  
 508  $R_{xA}$  divided by the integral taken above 10 GeV/c. This corresponds to the height of the peak in  $R_{xA}$  assuming that  
 509  $R_{xA}$  at high  $p_T$  is indeed unity. In these ratios the systematic uncertainties largely cancel. The values are  $1.06 \pm 0.09$ ,  
 510  $1.25 \pm 0.11$ ,  $1.17 \pm 0.10$ , and  $1.17 \pm 0.12$  for  $p$ +Al,  $p$ +Au,  $d$ +Au, and  ${}^3\text{He}$ +Au, respectively. The value is smallest in  
 511  $p$ +Al collisions and most pronounced in  $p$ +Au collisions. In addition, the maximum in  $R_{xA}$  moves towards higher  $p_T$   
 512 with increasing system size from 3.25 GeV/c in  $p$ +Al to 4.25 GeV/c in  $p$ +Au and  $d$ +Au to 5.25 GeV/c in  ${}^3\text{He}$ +Au.  
 513 The values are approximately the same as the peak heights calculated in fixed target  $p$ +A experiments [47] and as  
 514 originally predicted for RHIC energies [11, 14, 15]. However, the systematic trend with system size does not follow  
 515 the dependence observed at fixed target energies [8],

$$\frac{d\sigma_{xA}}{dp_T} = (xA)^{n(p_T)} \times \frac{d\sigma_{pp}}{dp_T}, \quad (2)$$

516 with a common exponent  $n(p_T)$  for a given  $\sqrt{s}$ . Here,  $xA$  stands for the product of the number of nucleons in the  
 517 small and large ions. Eq. 2 is re-written in terms of per event yield by factoring out the inelastic cross sections  $\sigma_{xA}^{\text{inel}}$   
 518 and  $\sigma_{pp}^{\text{inel}}$ :

$$\frac{dN_{xA}}{dp_T} = (xA)^{n(p_T)} \times \frac{\sigma_{pp}^{\text{inel}}}{\sigma_{xA}^{\text{inel}}} \times \frac{dN_{pp}}{dp_T}. \quad (3)$$

519 In the case of no nuclear modification for hard scattering processes, the per event yields in  $x$ +A and  $p$ + $p$  collisions  
 520 are related through the number of binary nucleon-nucleon collisions  $N_{\text{coll}}$ . In this case the exponent  $n(p_T) = 1$  and  
 521  $N_{\text{coll}}$  is:

$$\langle N_{\text{coll}} \rangle = xA \times \frac{\sigma_{pp}^{\text{inel}}}{\sigma_{xA}^{\text{inel}}}. \quad (4)$$

522 This identity can be used to relate the nuclear-modification factor,  $R_{xA}$ , and the exponent  $n(p_T)$ :

$$n(p_T) = 1 + \frac{\log(R_{xA})}{\log(xA)}. \quad (5)$$

523 The exponent  $n(p_T)$  is calculated from the ratio of  $R_{p\text{Au}}/R_{p\text{Al}}$  and  $R_{\text{HeAu}}/R_{p\text{Au}}$ . The uncertainties due to the  $p$ + $p$   
 524 cross section cancel in the ratios; so do most of the uncertainties on the  $N_{\text{coll}}$  calculation. The results are shown in  
 525 Fig. 8. The data show that there is no universal  $n(p_T)$  at  $\sqrt{s_{NN}} = 200$  GeV below 8–10 GeV/c. At higher  $p_T$ , the  
 526 common  $n(p_T)$  underlines the similarity of  $R_{xA}$  for all collision systems.

#### 527 4. $R_{xA}$ Centrality Dependence

528 In Fig. 9,  $R_{xA}$  is shown for the different centrality selections from different collision systems. The scale uncertainty  
 529 from the  $p$ + $p$  reference and, to a large extent, the scale uncertainty due to  $N_{\text{coll}}$  only influences the scale of  $R_{xA}$ , but  
 530 not the relative differences between systems. The comparison reveals clear systematic trends of  $R_{xA}$  with centrality  
 531 and system size.

532 For  $p_T > 8$  GeV/c, the  $R_{xA}$  values remain constant at similar values for the same centrality selection from different  
 533 collision systems. However, the plateau value varies with centrality.  $R_{xA}$  is below unity in the more central collisions,  
 534 consistent with unity in the 20%–40% bin, and above or consistent with unity in the peripheral collisions. In the lower  
 535  $p_T$  range, the 0%–5% and 0%–20% selections exhibit a clear Cronin peak structure, similar to the 0%–100% case,  
 536 but more pronounced. The height of the peak is largest for  $p$ +Au. The height of the peak is system size dependent  
 537 and decreases from  $p$ +Au, to  $d$ +Au, to  ${}^3\text{He}$ +Au, i.e. with increasing size of the projectile nucleus. The peak is  
 538 smaller for  $p$ +Al than for  $p$ +Au, so it also seems to decrease with decreasing size of the target nucleus. In contrast,  
 539 in peripheral collisions all systems follow a common trend. Though there is a gradual change between central and  
 540 semi-peripheral collisions, it is not consistent between systems.

541 To better understand the trends, the average nuclear-modification factor  $\langle R_{xA} \rangle$  is calculated for two distinct  $p_T$   
 542 regions, above 8 GeV/c to represent the high  $p_T$  region and from  $4 < p_T < 6$  GeV/c to capture the peak of  $R_{xA}$ .  
 543 These  $\langle R_{xA} \rangle$  are studied as function of  $N_{\text{coll}}$  and  $N_{\text{coll}}/N_{\text{proj}}$  shown in Tab. II. Hard scattering processes are expected

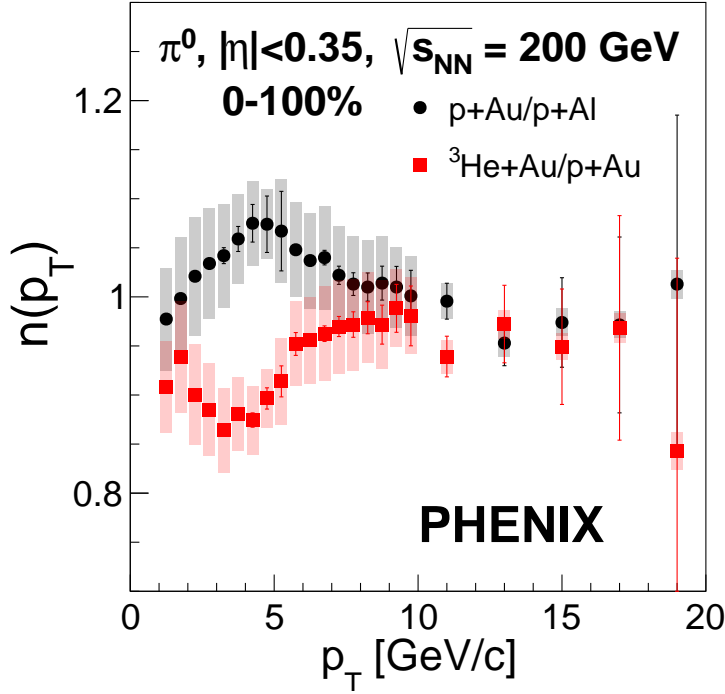


FIG. 8. Exponent according to Eq. 5 as a function of transverse momenta extracted from  $p$ +Au/ $p$ +Al and  $^3\text{He}$ +Au/ $p$ +Au collision systems. The uncertainties from the  $N_{\text{coll}}$  calculations and from the overall normalization of  $p$ + $p$  cancel in these ratios.

544 to scale with  $N_{\text{coll}}$ , thus  $N_{\text{coll}}$  is a natural choice. If the nucleons in the projectile interact independently with the  
 545 target nucleus, nuclear modifications should not depend on  $N_{\text{coll}}$ , but rather  $N_{\text{coll}}/N_{\text{proj}}$ . Note that  $N_{\text{coll}}$  and  $N_{\text{part}}$   
 546 are highly correlated and follow a common trend. In peripheral collisions, nucleons in the projectile are generally  
 547 striking unique nucleons in the target and  $N_{\text{part}} = N_{\text{coll}} + 1$  up to an  $N_{\text{coll}}$  value of  $\approx 14$ . For  $N_{\text{coll}} > 14$ ,  $N_{\text{part}}$  increases  
 548 slightly slower with  $N_{\text{coll}}$  as nucleons start to participate in multiple interactions. Consequently, common trends of a  
 549 nuclear modification with  $N_{\text{coll}}$  will also present themselves with respect to  $N_{\text{part}}$ . The  $\langle R_{xA} \rangle$  is calculated as follows:

$$\langle R_{xA} \rangle = \frac{\int \frac{dN_{xA}}{dp_T} dp_T}{N_{\text{coll}} \int \frac{dN_{pp}}{dp_T} dp_T} \quad (6)$$

550 Figure 10 shows  $\langle R_{xA} \rangle$  for the two  $p_T$  regions for all measured centrality selections from all collision systems. In  
 551 panels (a) and (b)  $\langle R_{xA} \rangle$  is plotted as function of  $N_{\text{coll}}$  and in panels (c) and (d) as function of  $N_{\text{coll}}$  per number of  
 552 participating nucleons in the projectile  $N_{\text{proj}}$ .

553 Figure 10(a) shows  $\langle R_{xA} \rangle$  as function of  $N_{\text{coll}}$  for the lower  $p_T$  range from 4 to 6 GeV/ $c$ , covering the peak in  $R_{xA}$   
 554 for all systems. The  $\langle R_{xA} \rangle$  is remarkably close to binary scaling, with deviations that are visibly smaller than those  
 555 observed at high  $p_T$  [see Fig. 10(b)]. Another notable difference compared to the high- $p_T$  range is that all systems  
 556 show similar deviations from binary scaling at the same  $N_{\text{coll}}$ . In contrast, the systems involving a Au target nucleus  
 557 do not show a common trend with  $N_{\text{coll}}/N_{\text{proj}}$  [see Fig. 10(c)] These observations are qualitatively the same for any  $p_T$   
 558 window between 1 and 6 GeV/ $c$ , which suggests that the mechanism underlying the nuclear modification is different  
 559 at high and low  $p_T$  with a transition in the 5 to 7 GeV/ $c$  range.

560 Figure 10(b) shows that for  $p_T$  above 8 GeV/ $c$  the  $\langle R_{xA} \rangle$  exhibits no common trend as function of  $N_{\text{coll}}$ . The  $\langle R_{xA} \rangle$   
 561 is below  $N_{\text{coll}}$  scaling for central classes and above for peripheral classes for all collision systems. The situation changes  
 562 when looking  $\langle R_{xA} \rangle$  versus  $N_{\text{coll}}/N_{\text{proj}}$  [see Fig. 10(d)]. The collision systems involving Au as a target nucleus ( $p$ +Au,  
 563  $d$ +Au, and  $^3\text{He}$ +Au) follow a common trend. For Al as a target nucleus, a distinctly different trend is observed. The  
 564 modifications to binary scaling or  $\langle R_{xA} \rangle$  remain approximately the same for similar  $p$ +Au and  $p$ +Al centrality classes,  
 565 but occur at different  $N_{\text{coll}}/N_{\text{proj}}$ . The same trends are observed for any choice of  $p_T$  threshold above 7 GeV/ $c$  up  
 566 to 15 GeV/ $c$ , above which the statistical precision is limited. There are two model independent conclusions that can

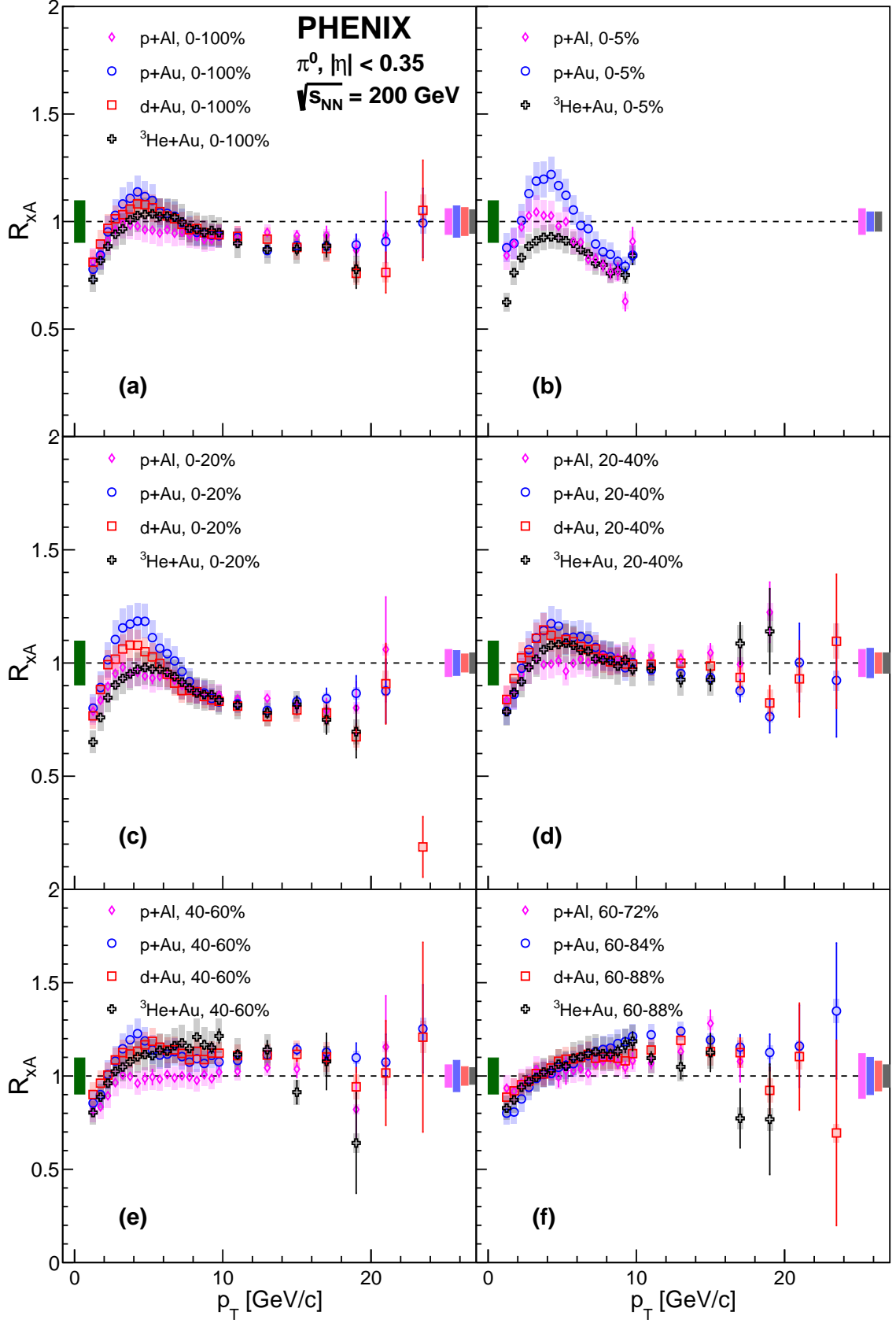


FIG. 9. Nuclear-modification factors in  $p+Al$ ,  $p+Au$ ,  $d+Au$ , and  ${}^3\text{He}+Au$  in 0%–100% and the five indicated centrality bins and for inelastic collisions at  $\sqrt{s_{NN}} = 200$  GeV. The error bars represent the statistical uncertainties, while the boxes represent the systematic uncertainties. The high- $p_T$  boxes are the uncertainties of the  $N_{\text{coll}}$  collisions from the Glauber model, while the low- $p_T$  box represents the overall normalization uncertainty from  $p+p$  collisions.

567 be derived from the observations: (i) the underlying mechanism for the nuclear modification does not depend on the  
 568 projectile nucleus, and (ii) the nuclear modification is not driven by the thickness of the nuclear matter traversed by  
 569 the projectile.

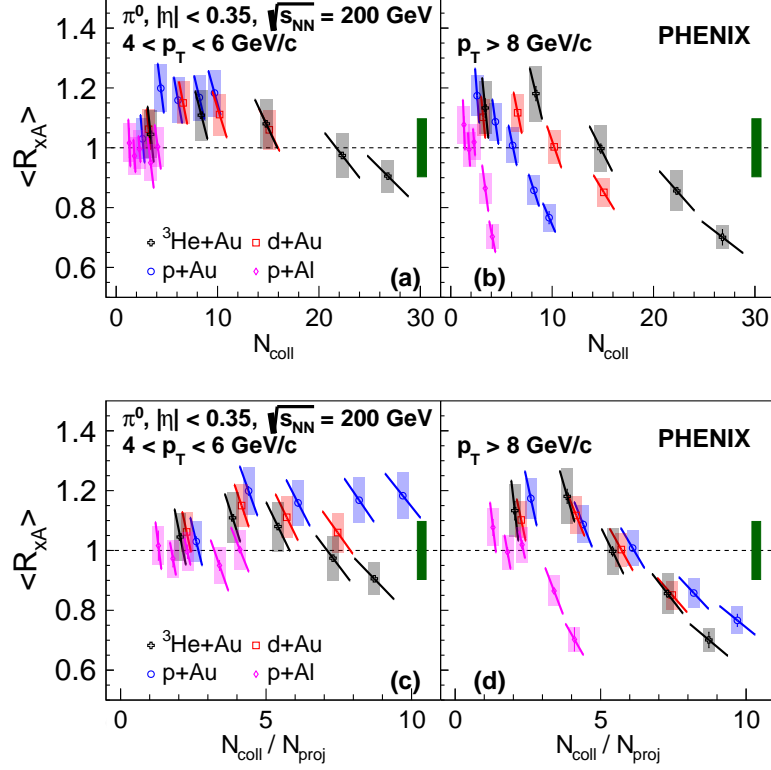


FIG. 10. Average  $R_{xA}$  versus the number of collisions for (a) the region around the  $R_{xA}$  peak [ $4 < p_T < 6 \text{ GeV}/c$ ] and (b) the high  $p_T$  region [ $p_T > 8 \text{ GeV}/c$ ]. (c,d) Average  $R_{xA}$  versus the number of collisions per projectile participant for the same two  $p_T$  ranges. The statistical (error bars) and systematic (boxes) uncertainties are indicated. The tilted error bars represent the anti-correlated uncertainty on the y and x-axis due to the  $N_{\text{coll}}$  calculations. The bar around unity at the highest  $p_T$  shown represents the overall normalization uncertainty from  $p+p$  collisions.

570

### 5. Model comparison and discussion

571 The PDF of a nucleon is modified if the nucleon is within a nucleus and the modifications increase with increasing  
 572 number of nucleons in the nucleus. Similarly to the free proton PDFs themselves, the nuclear parton distribution  
 573 functions (nPDFs) are determined empirically by fitting a large variety of experimental data. Here three different  
 574 nPDFs are considered: nNNPDFv1.0 [48], EPPS16 [49], and nCTEQ15 [50]. For consistency, the same framework  
 575 was used in all calculations with the same fragmentation function [51].

576 Figure 11 compares the measured nuclear-modification factors for inclusive  $p+\text{Al}$ ,  $p+\text{Au}$ ,  $d+\text{Au}$ , and  ${}^3\text{He}+\text{Au}$   
 577 collisions to the predictions using the three different nPDFs mentioned above. The central value of the predictions  
 578 is represented by a line and the uncertainties from fitting the nPDF to data are given as shaded area. Due to  
 579 their large uncertainties, all three nPDFs give  $R_{xA}$  predictions consistent with the data. However, looking at the  
 580 central values, the predictions are in tension with the trends of the data. For example, for the nNNPDF case  
 581 an enhancement is observed from 4 to above 20  $\text{GeV}/c$  for all systems, with a maximum near 8  $\text{GeV}/c$ , clearly not  
 582 consistent with data. Looking at individual collision systems, EPPS16 and nCTEQ15 based calculations qualitatively,  
 583 but not quantitatively, capture the general trends. The tension is most clearly visible when comparing the system  
 584 size dependence. Each nPDF calculation predicts an ordering of the enhancement of  $R_{xA}$  in their respective peak  
 585 region:  ${}^3\text{He}+\text{Au} > d+\text{Au} > p+\text{Au} > p+\text{Al}$ , which is significant as the systematic uncertainties on the nPDFs within  
 586 one approach are highly correlated between systems. The predicted ordering in the lower  $p_T$  (2–10  $\text{GeV}/c$ ) region,  
 587 depending on the model, results from the modification increasing both with the target size and with the projectile

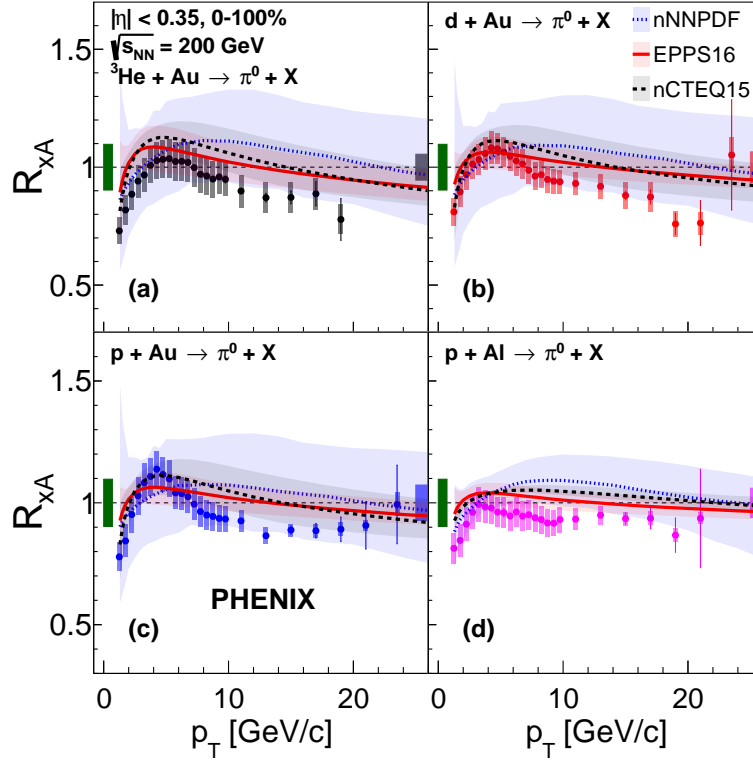


FIG. 11.  $R_{xA}$  for inelastic collisions compared to three different nuclear PDF calculations and their uncertainties. The data points include the statistical and systematic uncertainties. The left box around unity represents the overall normalization uncertainty on the  $p+p$  collisions and the right box represents the uncertainty from the calculated  $N_{\text{coll}}$ .

size. In contrast, the data show the reverse ordering  ${}^3\text{He}+\text{Au} < d+\text{Au} < p+\text{Au}$  with decreasing projectile size in the peak region.

For the same reasons that led to predictions of increasing modification at lower  $p_T$ . At high- $p_T$ , the models predict an ordering of  $R_{xA}$  with projectile and target size:  ${}^3\text{He}+\text{Au} < d+\text{Au} < p+\text{Au} < p+\text{Al}$ . In contrast, the data show a larger suppression than any of the models, and it is essentially independent of the collision system. However, given the systematic uncertainties on the  $R_{xA}$  scale, the nPDF predictions are consistent with the data at high  $p_T$ . The different trends, in particular at low  $p_T$ , of the nPDF calculations compared to the data suggest that there must be additional physics driving the nuclear modification beyond the nPDFs.

The data show that at high  $p_T$   $\pi^0$  yields from small systems are suppressed relative to  $p+p$  in central event selections, while they are enhanced for peripheral selections. Furthermore, for  $p+\text{Au}$ ,  $d+\text{Au}$ , and  ${}^3\text{He}+\text{Au}$ , the  $\langle R_{xA} \rangle$  values for  $p_T > 8 \text{ GeV}/c$  are consistent with a superposition of independent collisions of the projectile nucleons. At the same time,  $p+\text{Au}$  and  $p+\text{Al}$  show nearly the same  $\langle R_{xA} \rangle$  in the same centrality bin selection. These observations contradict any scenarios where parton energy loss would be responsible for the modification, which would necessarily result in an ordering of  $R_{xA}$  values as  ${}^3\text{He}+\text{Au} < d+\text{Au} < p+\text{Au} < p+\text{Al} \leq 1$  for the system dependence, with the suppression for each system being largest for central and  $R_{xA} \approx 1$  for peripheral collisions.

Models that invoke nucleon size variations have been proposed to explain the suppression/enhancement pattern seen in the data [33, 34]. These models assume that nucleons with high- $x$  partons have a more compact color configuration and thus will produce on average less binary collisions and target participants at the same impact parameter as nucleons without high- $x$  partons. As a consequence, events with a high  $p_T$   $\pi^0$  would typically be biased towards smaller multiplicity of the overall event, leading to an apparent enhancement in peripheral event selections and a suppression in central events. The calculations from [52], which predicted jet  $R_{xA}$  for  $p+\text{Au}$  and  ${}^3\text{He}+\text{Au}$  based on a comparison to  $d+\text{Au}$  data<sup>1</sup>, are compared to  $\pi^0$   $\langle R_{xA} \rangle$  above a  $p_T$  of  $8 \text{ GeV}/c$ , [see Fig. 12(a)]. The observed centrality

<sup>1</sup> Note that jet  $R_{xA}$  presented in [52] was converted to  $\pi^0$   $R_{xA}$  assuming  $p_T(\pi^0) = 0.7 p_T^{\text{jet}} = 0.7 \times 100 \text{ GeV} \times x_p$  and  $\langle R_{xA} \rangle \approx R_{xA}(p_T)$ . This procedure was discussed with the authors.

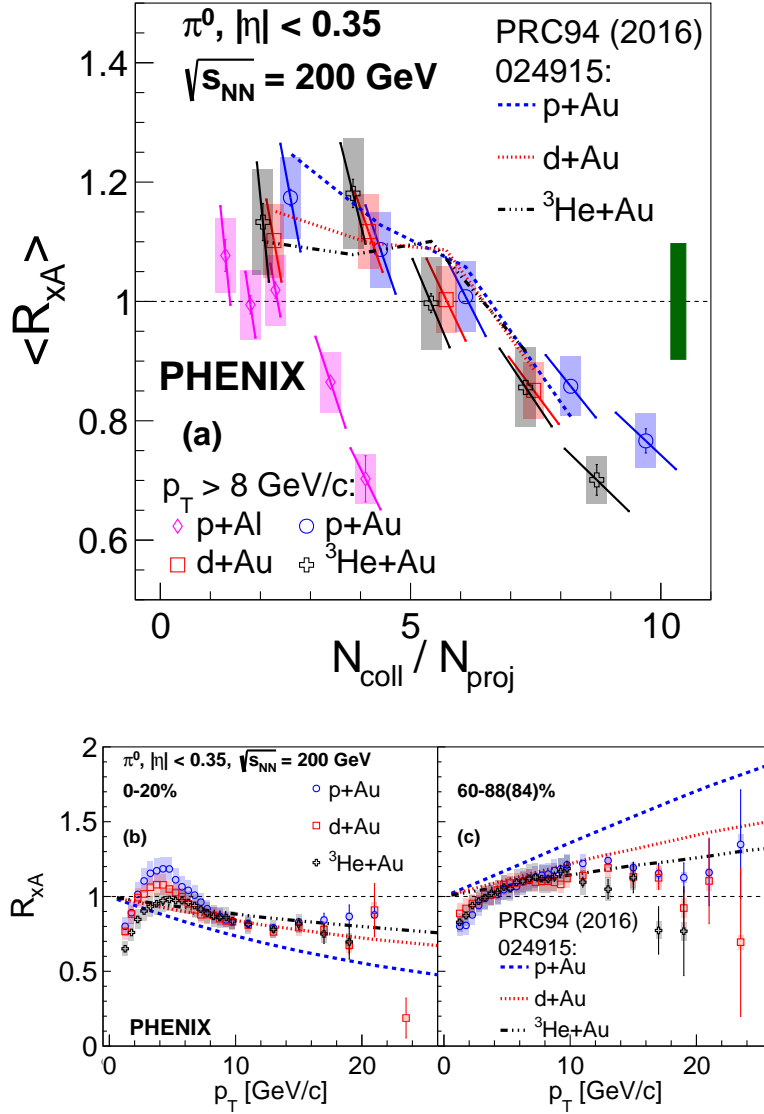


FIG. 12. (a) The  $\langle R_{xA} \rangle$  above  $p_T = 8$  GeV/c as a function  $N_{\text{coll}}/N_{\text{proj}}$  with predictions from [52] for the consequences of high- $x$  nucleon size fluctuations. (b) The  $R_{xA}$  as a function of  $p_T$  for (b) most-central and (c) most-peripheral collisions.

dependence is quite consistent with the data. It can be expected that in this model the same event selection bias would occur in  $p+\text{Al}$  collisions.

Although this model plausibly describes the  $d+\text{Au}$  and  $^3\text{He}+\text{Au}$  data, it particularly misses the  $p+\text{Au}$ . Additionally, it is important to note that this model predicts an ordering of  $R_{xA}$  with system size and centrality at higher  $p_T$ . Figure 12 clearly shows that for (b) central collisions the predicted  $R_{xA}$  values follow  $^3\text{He}+\text{Au} > d+\text{Au} > p+\text{Au}$  and for (c) peripheral collisions the ordering is reversed. In contrast, such an ordering is not supported by the data.

In Ref. [35], the bias of the event selection by centrality occurs because soft particle production away from the hard scattering process is suppressed, caused by the depletion of energy available in the projectile after the hard scattering process. The  $R_{xA}$  calculated for  $d+\text{Au}$  with this model was consistent with preliminary [35] and final  $d+\text{Au}$  data within systematic uncertainties. It would be interesting to see these calculations expanded to the full variety of available data from small systems.

In recent years particle spectra from  $p+p$  collisions at the LHC have been interpreted in the context of hydrodynamic models and the presence of strong radial flow [53–56], but no predictions exist for small systems at RHIC energies that could be compared to the data. If the large anisotropies of particle production seen at RHIC in  $p+\text{Au}$ ,  $d+\text{Au}$ ,

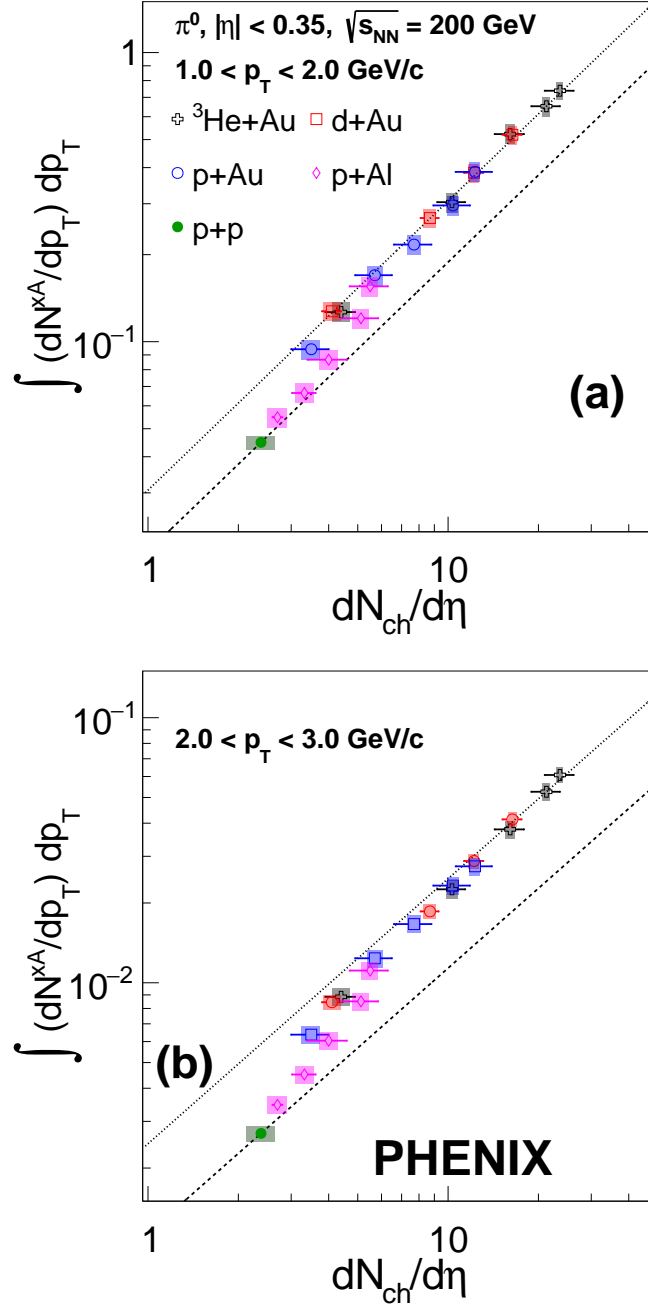


FIG. 13. Integrated yields for (a) 1–2 GeV/ $c$  and (b) 2–3 GeV/ $c$  as a function of charged particle multiplicity density at midrapidity. The lines are explained in the text.

624 and  $^3\text{He}+\text{Au}$  are indeed related to hydrodynamic expansion of the collision volume, as suggested in [27], then the  
 625 same systems must also exhibit radial flow because the anisotropy would be a geometry driven modulation of radial  
 626 flow. The effects of radial flow are typically most prominent at  $p_T$  below a few GeV/ $c$ , where soft particle production  
 627 mechanisms dominate. In the presence of radial flow the  $\pi^0$  yield would be shifted towards higher momentum by the  
 628 velocity field. Accordingly, when comparing the shape of the  $\pi^0$  momentum spectra from  $x+A$  to that from  $p+p$ , a  
 629 depletion of the yield at the lowest  $p_T$  is expected, while at higher  $p_T$  the yield would be enhanced with a transition  
 630 near the  $\pi^0$  mass. Because the  $p_T$  range of the  $\pi^0$  data starts at 1 GeV/ $c$ , only the region where an enhancement  
 631 would be expected can be studied here.

632 To look for possible indications of radial flow the integrated yields are calculated for two  $p_T$  ranges, 1–2 and 2–3  
 633 GeV/ $c$ , for all systems and event selections. The results are plotted in Fig. 13 as functions of the charged particle

634 multiplicity density  $dN_{\text{ch}}/d\eta$  at midrapidity for the corresponding system and event selection. Also shown on each  
 635 panel are two lines indicating integrated yields linearly increasing with  $dN_{\text{ch}}/d\eta$ . The lower line is anchored to the  
 636  $p+p$  point following a trend of unchanged shape of the spectra, and the upper line matches the yield for the 0%–20%  
 637  ${}^3\text{He}+\text{Au}$  selection. While the peripheral  $p+\text{Al}$  events follow the  $p+p$  trend, all other selections show higher integrated  
 638 yields compared to the  $p+p$  trend. Above  $dN_{\text{ch}}/d\eta \approx 10$  the data tends to be proportional to  $dN_{\text{ch}}/d\eta$  again but at  
 639 a much higher level.

640 The observed trend is qualitatively consistent with the presence of radial flow in small systems. Interestingly, the  
 641 surprisingly rapid transition over the  $dN_{\text{ch}}/d\eta$  range from  $\approx 3$  to 10 is similar to recent observations of low  $p_T$  direct  
 642 photon emission [57] and strangeness production [58]. Both also indicate a transition from  $p+p$ -like emission to a  
 643 significant enhancement at similar event multiplicities. Furthermore, the presence of radial flow could naturally explain  
 644 the much larger observed Cronin effect for protons from small systems [8], which so far has eluded a quantitative  
 645 understanding. However, before drawing firm conclusions, more investigations are necessary. These should include  
 646 the study of heavier hadrons, such as Kaons and protons.

## 647 VII. SUMMARY

648 In summary, this paper presents new measurements of the invariant cross section of neutral pion production from  
 649  $p+p$  collisions and invariant yields from  $p+\text{Al}$ ,  $p+\text{Au}$ ,  $d+\text{Au}$ , and  ${}^3\text{He}+\text{Au}$  at  $\sqrt{s_{NN}} = 200$  GeV. For  $p+p$  the new  
 650 results extend the measured range up to  $p_T \approx 25$  GeV/ $c$  and improve statistical and systematic uncertainties compared  
 651 to the previous measurement. NLO pQCD calculations are found to be consistent with the data as previously reported.  
 652 For  $p+\text{Al}$ ,  $p+\text{Au}$ ,  $d+\text{Au}$ , and  ${}^3\text{He}+\text{Au}$  collisions at  $\sqrt{s_{NN}} = 200$  GeV,  $\pi^0$   $p_T$  spectra from inelastic collisions and from  
 653 centrality selected event samples were measured, including a sample of the 0%–5% most central events for  $p+\text{Al}$ ,  
 654  $p+\text{Au}$ , and  ${}^3\text{He}+\text{Au}$ , which was recorded with a dedicated high multiplicity trigger.

655 At high transverse momentum ( $p_T > 8$  GeV/ $c$ ), where hard scattering processes are the dominant production mech-  
 656 anism, the nuclear modification factors for all collision systems are found to be nearly constant. For the same event  
 657 selection in percent centrality, different collision systems exhibit a value of  $R_{xA}$  that is compatible within uncertainties.  
 658 For the full inelastic cross section,  $R_{xA}$  is consistent with unity, pointing towards little or no nuclear modification of  
 659 hard scattering processes in small systems. For the most central events, it is observed that  $R_{xA}$  is significantly below  
 660 unity. However,  $R_{xA}$  increases monotonically with decreasing centrality and exceeds unity for peripheral collisions.  
 661 For Au target nuclei, the  $\langle R_{xA} \rangle$  above  $p_T$  of 8 GeV/ $c$  shows a common trend with  $N_{\text{coll}}/N_{\text{proj}}$ . This indicates that,  
 662 for hard scattering processes, the nucleons in the small projectile nucleus interact mostly independently with the Au  
 663 target. For  $p+\text{Al}$  collisions,  $\langle R_{xA} \rangle$  does not follow the same trend. At the same event centrality, the  $p+\text{Al}$   $\langle R_{xA} \rangle$  is  
 664 the same as for  $p+\text{Au}$ , which suggests that the mechanism that causes the change of  $R_{xA}$  with centrality does not  
 665 depend on the target nucleus.

666 These observations disfavor scenarios where energy loss is a significant contributor to the nuclear modification  
 667 of high  $p_T$  particle production in small systems. The counter-intuitive centrality dependence is likely linked to a  
 668 mismatch of the centrality selection of events using charged particle multiplicity and mapping them to a number of  
 669 binary collisions using the standard Glauber model. In this picture, events with a high  $p_T$   $\pi^0$  are biased towards  
 670 smaller underlying event multiplicity. This might be due to physical fluctuations of the proton size or simply due to  
 671 energy conservation if high  $p_T$  jets are present.

672 For lower  $p_T$ ,  $R_{xA}$  for all systems initially increases with  $p_T$  and reaches a peak near 4–6 GeV/ $c$  for central and  
 673 semi-central collisions. For peripheral collisions,  $R_{xA}$  levels off to a constant at approximately the same high  $p_T$  value  
 674 for all systems. For inelastic collisions and more central collisions,  $R_{xA}$  resembles what has been referred to as the  
 675 Cronin effect in fixed target experiments - a rise, followed by a peak, followed by a plateau. However, unlike at lower  
 676 energies,  $p+p$  and  $x+\text{A}$   $\pi^0$  cross sections are not related by a power  $(xA)^{n(p_T)}$  with a common  $n(p_T)$ . Furthermore,  
 677 the peak height value around 4–6 GeV/ $c$  shows a clear system size dependence  $p+\text{Au} > d+\text{Au} > {}^3\text{He}+\text{Au} > p+\text{Al}$ ,  
 678 where the  $R_{xA}$  peak height value is well above unity for  $p+\text{Au}$  and drops to close to unity for  $p+\text{Al}$  collisions.

679 While the shape of  $R_{xA}$  roughly resembles what is expected from the nuclear modification of PDFs, the observed  
 680 system size dependence of the peak height of  $R_{xA}$  shows exactly the reverse ordering of what was predicted by nPDF  
 681 calculations. Therefore it is likely that nPDFs alone are insufficient to explain the nuclear modifications in small  
 682 systems.

683 In the same  $p_T$  region,  $\langle R_{xA} \rangle$  was used to study the dependence on centrality. For all systems,  $\langle R_{xA} \rangle$  in the range  
 684 4–6 GeV/ $c$  follows a common trend with  $N_{\text{coll}}$ . At high  $p_T$ ,  $\langle R_{xA} \rangle$  scales with  $N_{\text{coll}}/N_{\text{proj}}$  for Au target nuclei. While  
 685 at lower  $p_T$ ,  $d+\text{Au}$  and  ${}^3\text{He}+\text{Au}$  are not a superposition of  $p+\text{Au}$ -like collisions. Consequently, different mechanisms  
 686 must contribute to the nuclear modification at high and low  $p_T$ . For high  $p_T$ , the apparent centrality dependence is  
 687 likely due to a bias in the event selection. At lower  $p_T$ , final state effects related to the presence of interacting hadrons  
 688 may be at play. If a QGP droplet is indeed produced during the collision, radial flow may be one possible mechanism

689 to explain this trend, although further investigation is needed that is outside the scope of this paper.

690

## ACKNOWLEDGMENTS

691 We thank the staff of the Collider-Accelerator and Physics Departments at Brookhaven National Laboratory and the  
 692 staff of the other PHENIX participating institutions for their vital contributions. We also thank I. Helenius and J. Rojo  
 693 for the nPDF calculations plus M. van Leeuwen for the NLO calculations. We acknowledge support from the Office  
 694 of Nuclear Physics in the Office of Science of the Department of Energy, the National Science Foundation, Abilene  
 695 Christian University Research Council, Research Foundation of SUNY, and Dean of the College of Arts and Sciences,  
 696 Vanderbilt University (U.S.A), Ministry of Education, Culture, Sports, Science, and Technology and the Japan Society  
 697 for the Promotion of Science (Japan), Conselho Nacional de Desenvolvimento Científico e Tecnológico and Fundação  
 698 de Amparo à Pesquisa do Estado de São Paulo (Brazil), Natural Science Foundation of China (People's Republic of  
 699 China), Croatian Science Foundation and Ministry of Science and Education (Croatia), Ministry of Education, Youth  
 700 and Sports (Czech Republic), Centre National de la Recherche Scientifique, Commissariat à l'Énergie Atomique,  
 701 and Institut National de Physique Nucléaire et de Physique des Particules (France), Bundesministerium für Bildung  
 702 und Forschung, Deutscher Akademischer Austausch Dienst, and Alexander von Humboldt Stiftung (Germany), J.  
 703 Bolyai Research Scholarship, EFOP, the New National Excellence Program (ÚNKP), NKFIH, and OTKA (Hungary),  
 704 Department of Atomic Energy and Department of Science and Technology (India), Israel Science Foundation (Israel),  
 705 Basic Science Research and SRC(CENuM) Programs through NRF funded by the Ministry of Education and the  
 706 Ministry of Science and ICT (Korea). Physics Department, Lahore University of Management Sciences (Pakistan),  
 707 Ministry of Education and Science, Russian Academy of Sciences, Federal Agency of Atomic Energy (Russia), VR  
 708 and Wallenberg Foundation (Sweden), the U.S. Civilian Research and Development Foundation for the Independent  
 709 States of the Former Soviet Union, the Hungarian American Enterprise Scholarship Fund, the US-Hungarian Fulbright  
 710 Foundation, and the US-Israel Binational Science Foundation.

- 
- 711 [1] K. Adcox *et al.* (PHENIX Collaboration), Suppression of hadrons with large transverse momentum in central Au+Au  
 712 collisions at  $\sqrt{s_{NN}} = 130$  GeV, *Phys. Rev. Lett.* **88**, 022301 (2002).  
 713 [2] C. Adler *et al.* (STAR Collaboration), Centrality dependence of high  $p_T$  hadron suppression in Au+Au collisions at  
 714  $\sqrt{s_{NN}} = 130$  GeV, *Phys. Rev. Lett.* **89**, 202301 (2002).  
 715 [3] S. S. Adler *et al.* (PHENIX Collaboration), Nuclear effects on hadron production in  $d$ +Au and  $p$ + $p$  collisions at  $\sqrt{s_{NN}} = 200$   
 716 GeV, *Phys. Rev. C* **74**, 024904 (2006).  
 717 [4] J. Adams *et al.* (STAR Collaboration), Evidence from  $d$ +Au measurements for final state suppression of high  $p_T$  hadrons  
 718 in Au+Au collisions at RHIC, *Phys. Rev. Lett.* **91**, 072304 (2003).  
 719 [5] A. Adare *et al.* (PHENIX Collaboration), Suppression pattern of neutral pions at high transverse momentum in Au+Au  
 720 collisions at  $\sqrt{s_{NN}} = 200$  GeV and constraints on medium transport coefficients, *Phys. Rev. Lett.* **101**, 232301 (2008).  
 721 [6] B. I. Abelev *et al.* (STAR Collaboration), Neutral Pion Production in Au+Au Collisions at  $\sqrt{s_{NN}} = 200$  GeV, *Phys. Rev.*  
 722 *C* **80**, 044905 (2009).  
 723 [7] J. W. Cronin, H. J. Frisch, M. J. Shochet, J. P. Boymond, R. Mermod, P. A. Piroue, and R. L. Sumner, Production of  
 724 hadrons with large transverse momentum at 200, 300, and 400 GeV, *Phys. Rev. D* **11**, 3105 (1975).  
 725 [8] D. Antreasyan, J. W. Cronin, H. J. Frisch, M. J. Shochet, L. Kluberg, P. A. Piroue, and R. L. Sumner, Production of  
 726 Hadrons at Large Transverse Momentum in 200, 300, and 400 GeV  $pp$  and  $pn$  Collisions, *Phys. Rev. D* **19**, 764 (1979).  
 727 [9] J. H. Kuhn, Nucleon Number Dependence of Large Transverse Momentum Reactions and Multiple Scattering, *Phys. Rev.*  
 728 *D* **13**, 2948 (1976).  
 729 [10] M. Lev and B. Petersson, Nuclear Effects at Large Transverse Momentum in a QCD Parton Model, *Z. Phys. C* **21**, 155  
 730 (1983).  
 731 [11] X.-N. Wang, Systematic study of high  $p_T$  hadron spectra in  $pp$ ,  $pA$ , and  $AA$  collisions from SPS to RHIC energies, *Phys.*  
 732 *Rev. C* **61**, 064910 (2000).  
 733 [12] Y. Zhang, G. I. Fai, G. Papp, G. G. Barnafoldi, and P. Levai, High  $p_T$  pion and kaon production in relativistic nuclear  
 734 collisions, *Phys. Rev. C* **65**, 034903 (2002).  
 735 [13] B. Z. Kopeliovich, J. Nemchik, A. Schafer, and A. V. Tarasov, Cronin effect in hadron production off nuclei, *Phys. Rev.*  
 736 *Lett.* **88**, 232303 (2002).  
 737 [14] A. Accardi and D. Treleani, Minijet transverse spectrum in high-energy hadron nucleus collisions, *Phys. Rev. D* **64**, 116004  
 738 (2001).  
 739 [15] I. Vitev and M. Gyulassy, High  $p_T$  tomography of  $d$ +Au and Au+Au at SPS, RHIC, and LHC, *Phys. Rev. Lett.* **89**,  
 740 252301 (2002).  
 741 [16] D. Kharzeev, Y. V. Kovchegov, and K. Tuchin, Cronin effect and high- $p_T$  suppression in  $pA$  collisions, *Phys. Rev. D* **68**,  
 742 094013 (2003).

- 743 [17] R. C. Hwa and C. B. Yang, Final state interaction as the origin of the Cronin effect, *Phys. Rev. Lett.* **93**, 082302 (2004).
- 744 [18] V. Khachatryan *et al.* (CMS Collaboration), Observation of Long-Range Near-Side Angular Correlations in Proton-Proton  
745 Collisions at the LHC, *J. High Energy Phys.* **09** (2010) 091.
- 746 [19] B. Abelev *et al.* (ALICE Collaboration), Long-range angular correlations on the near and away side in  $p$ -Pb collisions at  
747  $\sqrt{s_{NN}} = 5.02$  TeV, *Phys. Lett. B* **719**, 29 (2013).
- 748 [20] G. Aad *et al.* (ATLAS Collaboration), Observation of Associated Near-Side and Away-Side Long-Range Correlations in  
749  $\sqrt{s_{NN}} = 5.02$  TeV Proton-Lead Collisions with the ATLAS Detector, *Phys. Rev. Lett.* **110**, 182302 (2013).
- 750 [21] S. Chatrchyan *et al.* (CMS Collaboration), Observation of long-range near-side angular correlations in proton-lead collisions  
751 at the LHC, *Phys. Lett. B* **718**, 795 (2013).
- 752 [22] A. Adare *et al.* (PHENIX Collaboration), Quadrupole Anisotropy in Dihadron Azimuthal Correlations in Central  $d$ +Au  
753 Collisions at  $\sqrt{s_{NN}} = 200$  GeV, *Phys. Rev. Lett.* **111**, 212301 (2013).
- 754 [23] A. Adare *et al.* (PHENIX Collaboration), Measurements of elliptic and triangular flow in high-multiplicity  $^3\text{He}$ +Au colli-  
755 sions at  $\sqrt{s_{NN}} = 200$  GeV, *Phys. Rev. Lett.* **115**, 142301 (2015).
- 756 [24] C. Aidala *et al.* (PHENIX Collaboration), Measurement of long-range angular correlations and azimuthal anisotropies in  
757 high-multiplicity  $p$ +Au collisions at  $\sqrt{s_{NN}} = 200$  GeV, *Phys. Rev. C* **95**, 034910 (2017).
- 758 [25] C. Aidala *et al.* (PHENIX Collaboration), Measurements of Multiparticle Correlations in  $d$ +Au Collisions at 200, 62.4, 39,  
759 and 19.6 GeV and  $p$ +Au Collisions at 200 GeV and Implications for Collective Behavior, *Phys. Rev. Lett.* **120**, 062302  
760 (2018).
- 761 [26] A. Adare *et al.* (PHENIX Collaboration), Measurements of mass-dependent azimuthal anisotropy in central  $p$ +Au,  $d$ +Au,  
762 and  $^3\text{He}$ +Au collisions at  $\sqrt{s_{NN}} = 200$  GeV, *Phys. Rev. C* **97**, 064904 (2018).
- 763 [27] C. Aidala *et al.* (PHENIX Collaboration), Creation of quark-gluon plasma droplets with three distinct geometries, *Nature*  
764 *Phys.* **15**, 214 (2019).
- 765 [28] G. Aad *et al.* (ATLAS Collaboration), Transverse momentum and process dependent azimuthal anisotropies in  $\sqrt{s_{NN}} = 8.16$   
766 TeV  $p$ +Pb collisions with the ATLAS detector, *Eur. Phys. J. C* **80**, 73 (2020).
- 767 [29] A. Adare *et al.* (PHENIX Collaboration), Centrality categorization for  $R_{p(d)+A}$  in high-energy collisions, *Phys. Rev. C* **90**,  
768 034902 (2014).
- 769 [30] G. Aad *et al.* (ATLAS Collaboration), Centrality and rapidity dependence of inclusive jet production in  $\sqrt{s_{NN}} = 5.02$  TeV  
770 proton-lead collisions with the ATLAS detector, *Phys. Lett. B* **748**, 392 (2015).
- 771 [31] A. Adare *et al.* (PHENIX Collaboration), Centrality-dependent modification of jet-production rates in deuteron-gold  
772 collisions at  $\sqrt{s_{NN}} = 200$  GeV, *Phys. Rev. Lett.* **116**, 122301 (2016).
- 773 [32] Z.-B. Kang, I. Vitev, and H. Xing, Effects of cold nuclear matter energy loss on inclusive jet production in  $p$ +A collisions  
774 at energies available at the BNL Relativistic Heavy Ion Collider and the CERN Large Hadron Collider, *Phys. Rev. C* **92**,  
775 054911 (2015).
- 776 [33] M. Alvioli, B. A. Cole, L. Frankfurt, D. V. Perepelitsa, and M. Strikman, Evidence for  $x$ -dependent proton color fluctuations  
777 in  $p$ A collisions at the CERN Large Hadron Collider, *Phys. Rev. C* **93**, 011902(R) (2016).
- 778 [34] M. Alvioli, L. Frankfurt, D. V. Perepelitsa, and M. Strikman, Global analysis of color fluctuation effects in proton- and  
779 deuteron-nucleus collisions at RHIC and the LHC, *Phys. Rev. D* **98**, 071502(R) (2018).
- 780 [35] M. Kordell and A. Majumder, Jets in  $d(p)$ -A Collisions: Color Transparency or Energy Conservation, *Phys. Rev. C* **97**,  
781 054904 (2018).
- 782 [36] A. Adare *et al.* (PHENIX Collaboration), Inclusive cross-section and double helicity asymmetry for  $\pi^0$  production in  $p$ + $p$   
783 collisions at  $\sqrt{s_{NN}} = 200$  GeV: Implications for the polarized gluon distribution in the proton, *Phys. Rev. D* **76**, 051106  
784 (2007).
- 785 [37] L. Aphecetche *et al.* (PHENIX Collaboration), PHENIX calorimeter, *Nucl. Instrum. Methods Phys. Res., Sect. A* **499**,  
786 521 (2003).
- 787 [38] R. Brun, R. Hagelberg, M. Hansroul, and J. C. Lassalle, Geant: Simulation Program for Particle Physics Experiments.  
788 User Guide and Reference Manual (1978), CERN-DD-78-2-REV, CERN-DD-78-2.
- 789 [39] S. S. Adler *et al.* (PHENIX Collaboration), A Detailed Study of High- $p_T$  Neutral Pion Suppression and Azimuthal  
790 Anisotropy in Au+Au Collisions at  $\sqrt{s_{NN}} = 200$  GeV, *Phys. Rev. C* **76**, 034904 (2007).
- 791 [40] A. Adare *et al.* (PHENIX Collaboration), Pseudorapidity Dependence of Particle Production and Elliptic Flow in Asym-  
792 metric Nuclear Collisions of  $p$ +Al,  $p$ +Au,  $d$ +Au, and  $^3\text{He}$ +Au at  $\sqrt{s_{NN}} = 200$  GeV, *Phys. Rev. Lett.* **121**, 222301  
793 (2018).
- 794 [41] B. Alver, M. Baker, C. Loizides, and P. Steinberg, The PHOBOS Glauber Monte Carlo, arXiv:0805.4411.
- 795 [42] L. Lyons, D. Gibaut, and P. Clifford, How to Combine Correlated Estimates of a Single Physical Quantity, *Nucl. Instrum.*  
796 *Methods Phys. Res., Sect. A* **270**, 110 (1988).
- 797 [43] A. Valassi, Combining correlated measurements of several different physical quantities, *Nucl. Instrum. Methods Phys. Res.,*  
798 *Sect. A* **500**, 391 (2003).
- 799 [44] A. Valassi and R. Chierici, Information and treatment of unknown correlations in the combination of measurements using  
800 the BLUE method, *Eur. Phys. J. C* **74**, 2717 (2014).
- 801 [45] B. Jager, A. Schafer, M. Stratmann, and W. Vogelsang, Next-to-leading order QCD corrections to high- $p_T$  pion production  
802 in longitudinally polarized  $pp$  collisions, *Phys. Rev. D* **67**, 054005 (2003).
- 803 [46] M. L. Miller, K. Reygers, S. J. Sanders, and P. Steinberg, Glauber modeling in high energy nuclear collisions, *Ann. Rev.*  
804 *Nucl. Part. Sci.* **57**, 205 (2007).
- 805 [47] P. B. Straub, D. E. Jaffe, H. D. Glass, M. R. Adams, C. N. Brown, G. Charpak, *et al.*, Nuclear dependence of high- $x_t$

- 806 hadron and high- $Tau$  hadron-pair production in  $pA$  interactions at  $\sqrt{s} = 38.8$  GeV, Phys. Rev. Lett. **68**, 452 (1992).
- 807 [48] R. Abdul Khalek, J. J. Ethier, and J. Rojo (NNPDF Collaboration), Nuclear parton distributions from lepton-nucleus  
808 scattering and the impact of an electron-ion collider, Eur. Phys. J. C **79**, 471 (2019).
- 809 [49] K. J. Eskola, P. Paakkinen, H. Paukkunen, and C. A. Salgado, EPPS16: Nuclear parton distributions with LHC data,  
810 Eur. Phys. J. C **77**, 163 (2017).
- 811 [50] K. Kovarik *et al.*, nCTEQ15- Global analysis of nuclear parton distributions with uncertainties in the CTEQ framework,  
812 Phys. Rev. D **93**, 085037 (2016).
- 813 [51] D. de Florian, M. Epele, R. J. Hernandez-Pinto, R. Sassot, and M. Stratmann, Parton-to-Kaon Fragmentation Revisited,  
814 Phys. Rev. D **95**, 094019 (2017).
- 815 [52] D. McGlinchey, J. L. Nagle, and D. V. Perepelitsa, Consequences of high- $x$  proton size fluctuations in small collision  
816 systems at  $\sqrt{s_{NN}} = 200$  GeV, Phys. Rev. C **94**, 024915 (2016).
- 817 [53] T. Bhattacharyya, J. Cleymans, A. Khuntia, P. Pareek, and R. Sahoo, Radial Flow in Non-Extensive Thermodynamics  
818 and Study of Particle Spectra at LHC in the Limit of Small  $(q - 1)$ , Eur. Phys. J. A **52**, 30 (2016).
- 819 [54] D. Sarkar, S. Choudhury, and S. Chattopadhyay, Effect of radial flow on two particle correlations with identified triggers  
820 at intermediate  $p_T$  in  $p$ -Pb collisions at  $\sqrt{s_{NN}} = 5.02$  TeV, Phys. Lett. B **760**, 763 (2016).
- 821 [55] Y. Hirono and E. Shuryak, Femtosopic Signature of Strong Radial Flow in High-multiplicity  $pp$  Collisions, Eur. Phys. J.  
822 Web Conf. **141**, 01008 (2017).
- 823 [56] A. Khuntia, H. Sharma, S. Kumar Tiwari, R. Sahoo, and J. Cleymans, Radial flow and differential freeze-out in proton-  
824 proton collisions at  $\sqrt{s} = 7$  TeV at the LHC, Eur. Phys. J. A **55**, 3 (2019).
- 825 [57] A. Adare *et al.* (PHENIX Collaboration), Beam Energy and Centrality Dependence of Direct-Photon Emission from  
826 Ultrarelativistic Heavy-Ion Collisions, Phys. Rev. Lett. **123**, 022301 (2019).
- 827 [58] J. Adam *et al.* (ALICE Collaboration), Enhanced production of multi-strange hadrons in high-multiplicity proton-proton  
828 collisions, Nature Phys. **13**, 535 (2017).